TECHNICAL REPORT

PAMARCMiP Contribution

An analytic model companion based on observations: The role of low-level jets in the advection of passive tracers in the high Arctic

Olaf Hellmuth[1,*], Ulrike Egerer[1], Holger Siebert[1], and Lise Lotte Sørensen[2]

[1]*Leibniz Institute for Tropospheric Research, Permoserstr. 15, 04318 Leipzig, Leibniz-Sozietät der Wissenschaften zu Berlin e. V., Langenbeck-Virchow-Haus, Luisenstrasse 58/59, 10117 Berlin, Germany*
[2]*Aarhus University, Nordre Ringgade 1, 8000 Aarhus C, Denmark*
[*]*Corresponding author: Olaf Hellmuth, olaf.hellmuth@tropos.de*

March 1, 2023

Contents

Summary

The present report povides technical background information to the study of Egerer et al. (2023) on the role of a low-level jet (LLJ) for stirring the stable atmospheric surface layer in the Arctic. Based on micrometeorological tower measurements and tethered balloon-borne hot-wire anemometer measurements conducted during a 15 h observation period during the PAMARCMiP field experiment at the Villum Research Station (VRS, Station Nord) in North-East Greenland (March 28-30, 2018) (Hendriksen (ed.) 2019, p. 9, Fig. 4.2 therein), Egerer et al. (2023) analyzed the transition of a stable atmospheric boundary layer (ABL) with a LLJ into a traditional stable ABL in the late-winter central Arctic.

To support the conclusions drawn in Egerer et al. (2023) the present report contains

- supporting material on the LLJ phenomenology (**Section 1**),
- details of the evaluation of the tower measurements for the characterization of the atmospheric stability within the framework of the Monin-Obukhov theory (**Section 2**),
- a brief description of the analytical Shapiro-Fedorovich LLJ model (**Section 3**),
- a first guess-estimation of the partial process contributions to the time rate of change of the turbulent kinetic energy (**Section 4**), and
- a 2D model-based analysis of the potential role that LLJs can play in the local aerosol transport (**Section 5**).

1 Low-level jet phenomenology

1.1 General phenomenology

A low-level jet (LLJ) is a relaxation phenomenon of the wind in the atmospheric boundary layer (ABL) emerging during the transition from an initial ageostrophic equilibrium (between pressure gradient, Coriolis, and turbulent friction forces) to a final geostrophic equilibrium (between pressure gradient and Coriolis forces). It typically starts to develop around sunset at conditions of very strong thermal stratification, reaching its maximum in the early morning hours, and disappearing with sunrise by onset of daytime convective mixing (e.g., Blackadar 1957; Thorpe and Guymer 1977; Mix 1981; Beyrich and Klose 1987; Heinemann 2004; Shapiro and Fedorovich 2010. Favourable conditions for the development of a LLJ are clear-sky conditions with negative radiation balance (strong radiative cooling of the surface and low atmospheric backradiation). The LLJ is characterized by an anticyclonic turning of the wind vector with time, and the development of a pronounced wind maximum at altitudes of less than $1\,\mathrm{km}$, frequently occurring at heights $z < 500\,\mathrm{m}$; the maximum wind velocity is reported to often exceed the geostrophic wind by $\geq 70\,\%$ (Shapiro and Fedorovich 2010). The LLJ exhibits two characteristic phases (Shapiro and Fedorovich 2010):

- The pre-LLJ phase prevails during daytime and is characterized by a stationary atmospheric flow obeying ageostrophic equilibrium between three forces: the horizontal pressure gradient force, the Coriolis force, and the frictional force (originating from turbulent stress). The resulting wind profile is known as Ekman spiral. At the surface, the wind follows Buys Ballot's law, also known as baric wind law[1], turning anticyclonically with height from the ground to the top of the ABL, where the turbulent friction attains its minimum, resulting in a quasi-geostrophic wind.

- The LLJ phase typically starts at sunset ($t = 0$) under clear-sky and dry conditions. In this phase radiative cooling causes a near-surface temperature inversion, which in turn leads to a downward directed sensible heat flux in the Prandtl layer and a rapid decay of the vertical mixing in the ABL. The sudden disappearance of turbulent friction results in an imbalance of the initial ageostrophic force equilibrium, which in turn causes an acceleration of air parcels to finally achieve a new, geostrophic force equilibrium. Then the quasi-inviscid flow undergoes an inertial oscillation with a period length of $\tau = 2\pi/f$, where $f = 2\Omega\sin\varphi$ denotes the Coriolis parameter, $\Omega = 2\pi/T = 7.2921{\cdot}10^{-5}\,\mathrm{s}^{-1}$ the angular velocity of the Earth, $T = 23\,\mathrm{h}\,56\,\mathrm{min}\,4.1\,\mathrm{s}$ the rotation period of the Earth (one sidereal day), and φ the geographic latitude.

LLJ generation is determined by both geographic and hydrothermodynamic drivers. Geographic drivers are the orography, the slope of the terrain, the spatial distribution of land and water surfaces, and the geographic latitude. Hydrothermodynamic drivers comprise the curvature of the streamlines, the thermal stability of the atmosphere, the diurnal

[1] In the Northern Hemisphere, if an observer turns his back to the wind, the low pressure center will be located to the left and somewhat toward the front, while the high pressure system will be located to the right and somwhat toward the back.

cycle of thermal stability and the eddy diffusivity of the atmosphere, the baroclinity of the lower atmosphere, vertical advection (convection), and effects of nonstationarity of single meteorological observables (Beyrich and Klose 1987). Corresponding to the variety of its generating factors, the occurrence of LLJ is quite different over space and time. For Northern Germany Kottmeier et al. (1983) reported LLJ occurrence in $10.4\,\%$ of all nights. For North Africa Fiedler et al. (2013) estimated an frequency of occurrence of $29\,\%$ of all nights in the annual and spatial mean with a distinct annual cycle with marked regional differences. Maxima of up to $80\,\%$ frequency were found at coincidence of low-level baroclinicity and orographic channeling, e.g., over the Bodélé Depression, Chad, for November–February and along the West Saharan and Mauritanian coast for April–September. For the Arctic Ocean during the period from October 2019 through September 2020 López-García et al. (2022) found LLJ occurrence throughout the entire year with a mean annual frequency of occurrence of more than $40\,\%$ and some seasonal variability. During winter and the freeze-up period LLJs were found to be more common and faster with an average occurrence of $55\,\%$, while in summer and the transition period the mean occurrence amounted $46\,\%$, which is similar to the ERA5 reanalysis. On the base of ERA5 data over the full year and whole Arctic Ocean the authors found a strong dependence of the frequency of occurrence on both the season and the distance to the sea-ice edge. For six months in a one-year field campaign in 2014/2015 at the Tiksi observatory in the Laptev Sea area Heinemann et al. (2021) observed LLJ presence in about $23\,\%$ of all profiling data.

1.2 Peculiarities in polar regions

A stable ABL is the *conditio sine qua non* for LLJ occurrence. While in the mid-latitudes thermal stability is a temporary phenomenon in the continental ABL preferentially occurring at nighttime, over the ice sheets of the Antarctic and Greenland the stable ABL is a quasi-permanent phenomenon for most parts of the year (Heinemann 2004). Midlatitude and polar LLJs differ by the strengthness of their generating driving forces. Over polar regions, orographic effects may play a dominant role. The inclination of the ice sheets over large areas causes the development of katabatic winds, and the Coriolis force is important as well because of the relatively large extent of the wind system in horizontal directions (Heinemann 2004). Over the Greenlandic ice sheet Heinemann (2004) observed LLJ wind maxima of up to $25\,\mathrm{m\,s^{-1}}$. The strong wind shear associated with katabatic winds causes fully developed (mechanically induced) turbulence in the stable ABL (Heinemann 2004). An important finding for the description of polar LLJs in katabatic wind systems in the fully turbulent stable ABL over the polar ice sheet under the condition of strong baroclinicity is the applicability of the "mid-latidue" concept of local scaling or z-less scaling as introduced by Nieuwstadt (1984) (see also Heinemann 2004). From their observations of wintertime LLJs in the coastal region of the Laptev Sea in the Siberian Arctic Heinemann et al. (2021) concluded that baroclinity seems to be the main driving mechanism for LLJs, since no inertial oscillations were found.

2 Analysis of the atmospheric stability from tower measurements of wind and temperature

During PAMARCMiP at VRS, March 29, 2018, tower measurements of wind and temperature at two different heights, $z_1 = 9\,\mathrm{m}$ and $z_2 = 65\,\mathrm{m}$, were carried out. These data were used to estimate the time-averaged turbulent heat fluxes for both the pre-LLJ and LLJ phases. The pre-LLJ phase was defined to last from 03:00:00 LT to 10:00:00 LT, and the LLJ phase from 10:55:00 LT to 15:35:12 LT. The time-averaged turbulent heat flux (symbol $\langle\ \rangle$) at height z over the time interval Δt is defined as follows:

$$\langle\overline{w'\theta'}\rangle(z) = \frac{1}{\Delta t}\int\limits_{t_1}^{t_2} \overline{w'\theta'}(z,t)\,\mathrm{d}t\ . \tag{1}$$

Here, the quantity $\overline{w'\theta'}(z,t)$ is the actual value of the turbulent heat flux, which is determined from actual values of the friction velocity $u_\star(z,t)$ and the scaling temperature $\theta_\star(z_1,z_2,t)$ at two different heights:

$$\begin{aligned} \overline{w'\theta'}(z_1,t) &= -u_\star(z_1,t)\,\theta_\star(z_1,z_2,t)\ , \\ \overline{w'\theta'}_s(z_2,t) &= -u_\star(z_2,t)\,\theta_\star(z_1,z_2,t)\ . \end{aligned} \tag{2}$$

The quantities $u_\star$ and $\theta_\star$ are the friction velocity and the kinematic scaling temperature. While $u_\star$ is positive definite, $\theta_\star$ can change sign depending on atmospheric stability. Both quantities are determined within the framework of the Monin-Obukhov similarity theory using observed time series of the wind speed $u(z,t) = |\vec{u}(z,t)|$ at one height z, and of temperatures $T(z_1,t)$ and $T(z_2,t)$ at two levels z_1, z_2 (Holtslag 1987, Chapter III, Appendix A, Eqs. (A3), (A4) therein):

$$\begin{aligned} u_\star &= \frac{\kappa u(z)}{f_M(z_0,z,L)}\ , \\ f_M(z_0,z,L) &= \ln\left(\frac{z}{z_0}\right) - \Psi_M\left(\frac{z}{L}\right) + \Psi_M\left(\frac{z_0}{L}\right)\ , \end{aligned} \tag{3}$$

$$\begin{aligned} \theta_\star &= \frac{\kappa\Delta\theta}{f_H(z_1,z_2,L)}\ , \\ \Delta\theta &= \theta(z_2) - \theta(z_1) = T(z_2) - T(z_1) + \Gamma_a(z_2 - z_1)\ , \\ f_H(z_1,z_2,L) &= \ln\left(\frac{z_2}{z_1}\right) - \Psi_H\left(\frac{z_2}{L}\right) + \Psi_H\left(\frac{z_1}{L}\right)\ , \end{aligned} \tag{4}$$

$$L = \frac{u_\star^2}{\kappa\beta\theta_\star}\ . \tag{5}$$

Here, L denotes the Monin-Obukhov length (MOL), $\kappa = 0.35$ is the von-Karman constant, $\beta = g/\theta(z_1)$ is the buoyancy parameter, z_0 the aerodynamic roughness length, $\Gamma_a = g/c_{pa}$ the dry-adiabatic lapse rate, and Ψ_M and Ψ_H are the stability functions for

momentum and heat. For unstable conditions $(z/L < 0)$ these functions read (Holtslag 1987, Chapter III, Appendix A, Eqs. (A6)–(A8) therein):

$$\begin{aligned} \Psi_M\left(\frac{z}{L}\right) &= 2\ln\left(\frac{1+x}{2}\right) + \ln\left(\frac{1+x^2}{2}\right) - 2\arctan(x) + \frac{\pi}{2}\,, \\ \Psi_H\left(\frac{z}{L}\right) &= 2\ln\left(\frac{1+x^2}{2}\right)\,, \\ x &= \left(1 - 16\frac{z}{L}\right)^{1/4}\,. \end{aligned} \tag{6}$$

For very stable conditions $(0 \leq z/L \leq 10)$ the stability functions are given by the following relations (Holtslag 1987, Chapter IV, Eqs. (10)–(12) therein):

$$\begin{aligned} \Psi_M\left(\frac{z}{L}\right) &= -\left[a\frac{z}{L} + b\left(\frac{z}{L} - \frac{c}{d}\right)\exp\left(-d\frac{z}{L}\right) + \frac{bc}{d}\right]\,, \\ a &= 0.7\,, \quad b = 0.75\,, \quad c = 5\,, \quad d = 0.35\,, \\ \Psi_H\left(\frac{z}{L}\right) &= \Psi_M\left(\frac{z}{L}\right)\,. \end{aligned} \tag{7}$$

Sorbjan and Grachev (2010) emphasized that weak turbulence in a very stable ABL limits the validity of the Monin–Obukhov similarity theory. According to them the predictions of this theory for gradients are formally valid only for subcritical values of the Richardson number. Furthermore, similarity functions cannot be accurately estimated during very stable stratification due to uncertainties caused by small flux values, and due to serious self-correlation errors. The general extensibility of the validity of the similarity approach into the supercritical region remains unclear in view of a large scatter of observational points. However, due to lack of a suitable alternative the Monin–Obukhov similarity theory is applied in the present case.

For measured $T(z_1)$, $T(z_2)$, and $u(z)$ Eqs. (3), (4), and (5) (with the constraints set by Eqs. (6) and (7)) constitute a system of three equations for the determination of the three unknown variables $u_\star$, $\theta_\star$, and L. Inserting Eqs. (3) and (4) into Eq. (5) delivers a governing equation for the determination of L:

$$L = \frac{u_\star^2}{\kappa\beta\theta_\star} = \frac{|\vec{u}|^2}{\beta\Delta\theta}\left(\frac{f_H(z_1, z_2, L)}{f_M^2(z_0, z, L)}\right)\,. \tag{8}$$

This is a transcendental equation in the sought-after quantity L, which can be solved by numerical iteration. Knowing L, the quantity $u_\star$ is obtained from (3), and $\theta_\star$ from Eq. (4). Therewith, the kinematic heat flux $\overline{w'\theta'}$ becomes a uniquely determined quantity. For the roughness length a value of $z_0 = 1\,\mathrm{cm}$ (ice and snow) was adopted. The potential temperatures $\theta(z_1)$ and $\theta(z_2)$ entering Eq. (4) were evaluated at $z_1 = 9\,\mathrm{m}$ and $z_2 = 65\,\mathrm{m}$. The scaling properties L, $u_\star$, and $\theta_\star$, were determined for two different choices of the reference level of the measured wind velocity $u(z)$, i.e., optionally at $z = z_1$ and $z = z_2$. Approximating the turbulent heat flux by the small-eddy (or down-gradient) ansatz, Eqs. (3) and (4) set the following constraint on the eddy diffusivity of heat K_H:

$$\overline{w'\theta'} = -u_\star\theta_\star \approx -K_H\frac{\Delta\theta}{\Delta z} \quad \rightsquigarrow \quad K_H(z) \approx \frac{\kappa^2 u(z_2 - z_1)}{f_M(z_0, z, L) f_H(z_1, z_2, L)}\,. \tag{9}$$

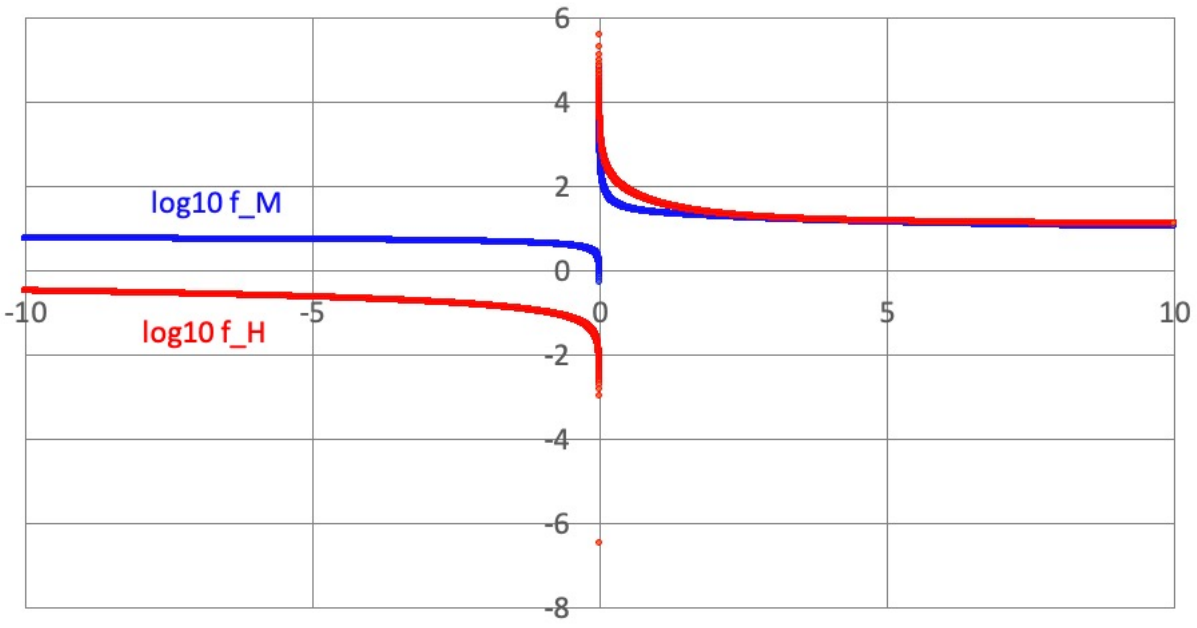

Figure 1: Decadic logarithms of the stability functions, $\log_{10} f_M(z_0, z, L)$ (blue graph) and $\log_{10} f_H(z_1, z_2, L)$ (orange graph), as functions of the Monin-Obuchov length L for $z = z_1$, $z_1 = 9\,\mathrm{m}$, $z_2 = 65\,\mathrm{m}$, and $z_0 = 0.01\,\mathrm{m}$.

Figure 1 shows the decadic logarithms of the stability functions, $\log_{10} f_M(z_0, z, L)$ (blue graph) and $\log_{10} f_H(z_1, z_2, L)$ (orange graph), as functions of L for $z = z_1$, $z_1 = 9\,\mathrm{m}$, $z_2 = 65\,\mathrm{m}$, and $z_0 = 0.01\,\mathrm{m}$. The functions $f_M(z_0, z, L)$ and $f_H(z_1, z_2, L)$ are positive definite quantities, decreasing to very small values upon the approaching the limit $-|L| \to 0$ for $L < 0$ (unstable stratification), while increasing to infinity upon approaching the limit $L \to 0$ for $L > 0$ (stable stratification),

$$\begin{aligned}
\lim_{L^+\to 0} u_\star(L) &= \lim_{L^+\to 0} \frac{\kappa|\vec{u}|}{f_M(z_0, z, L)} = 0\,, \\
\lim_{L^+\to 0} \theta_\star(L) &= \lim_{L^+\to 0} \frac{\kappa[\theta(z_2) - \theta(z_1)]}{f_H(z_1, z_2, L)} = 0 \quad \text{for} \quad \Delta\theta = \theta(z_2) - \theta(z_1) > 0 \\
\lim_{L^+\to 0} \overline{w'\theta'}(L) &= \lim_{L^+\to 0} \Big(- u_\star(L)\theta_\star(L) \Big) = 0\,.
\end{aligned}$$

As a consequence, upon decreasing L to zero in a thermally stable ABL, the downward directed vertical heatflux tends to zero too. **Figures 2** and **3** display the time series of $u(z,t)$ (in units of $\mathrm{m\,s^{-1}}$), $\vartheta(z,t)$ (in units of $^\circ\mathrm{C}$), and in **Figs. 4**, **5**, and **6** the calculated values of L, $u_\star$, and $\theta_\star$ are shown[2]. Both $u_\star$ and $\theta_\star$ are positive during the whole observation period, tending to larger values in the LLJ phase (enhanced stability). In **Fig. 7** the time series of the heat flux $\overline{w'\theta'} = -u_\star\theta_\star$ (in units of $\mathrm{K\,m\,s^{-1}}$) at $z_1 = 9\,\mathrm{m}$ and $z_2 = 65\,\mathrm{m}$

[2]The correctness of the computer implementation of the calculus for the determination of L, $u_\star$, and $\theta_\star$ has been checked by inserting the calculated parameters back into Eqs. (3) and (4) to recalculate the observed values of $u(z)$ and $\Delta\theta$. The R-squared statistics between the observed and recalculated values of $u(z)$ and $\Delta\theta$ were found to amount $R^2 = 1$ in all cases (not shown here).

is shown. The sensible heat fluxes during the pre-LLJ and LLJ phases were found to be negative with extremely small absolute values, indicating a tiny downward directed heat flux with a tendency to enhancement during the LLJ phase. **Figure 8** shows the time series of $K_H(z,t)$ (in units of $\mathrm{m^2\,s^{-1}}$), revealing enhanced values during the LLJ phase.

Table 1 shows the time-averaged values and the corresponding standard deviations of the scaling properties. Depending on the choice of the reference height for the wind velocity, $u(z_1)$ or $u(z_2)$, the scaling properties $\langle L\rangle$, $\langle u_\star\rangle$, $\langle\theta_\star\rangle$, the resulting heat flux $\langle\overline{w'\theta'}\rangle$, as well as $\langle K_H\rangle$ correspond either to $z=z_1$ or $z=z_2$. The time-averaged MOL was found to assume small positive values, $\langle L\rangle \gtrsim 0$, indicating a stable stratification. Upon transition from the pre-LLJ to the LLJ phase the stability of the stratification increases for both settings, $u(z)=u(z_1)$ and $u(z)=u(z_2)$. The increase in the layer stability by the pre-LLJ-to-LLJ-transition was found to be slightly more pronounced at the level z_2 compared to level z_1. The time-averaged friction velocity $u_\star$ is overall very small, weakly increasing upon the transition from the pre-LLJ to the LLJ phase, which is also more pronounced at $z=z_2$ compared to $z=z_1$. The time-averaged heat fluxes $\langle\overline{w'\theta'}\rangle$ at $z=z_1$ and $z=z_2$ were found to assume negative but very small absolute values.

Upon transition from the pre-LLJ to the LLJ phase the downward directed heat flux increases (by its absolute value) at $z=z_1$ by one order of magnitude, but at $z=z_2$ by three orders of magnitude. Hence, both the momentum and heat fluxes increase during the pre-LLJ-to-LLJ transition. This increase appeared slightly more pronounced at $z=z_2$ compared to $z=z_1$. Finally, the time-averaged eddy diffusivity $\langle K_H\rangle$ correlates well with the turbulent heat flux. The averaged value during the LLJ phase amounts $\langle K_H(z_2)\rangle = 0.024\,\mathrm{m^2\,s^{-1}}$ (with a standard deviation of $\sigma_{K_H}=0.037\,\mathrm{m^2\,s^{-1}}$). These findings indicate that the ABL evolution is nearly completely decoupled from the evolution of the surface layer not only during the LLJ phase but also already during the pre-LLJ phase. Hence, the observed LLJ might be also affected by factors not considered in the present modelling approach, such as orography-induced catabatic flows.

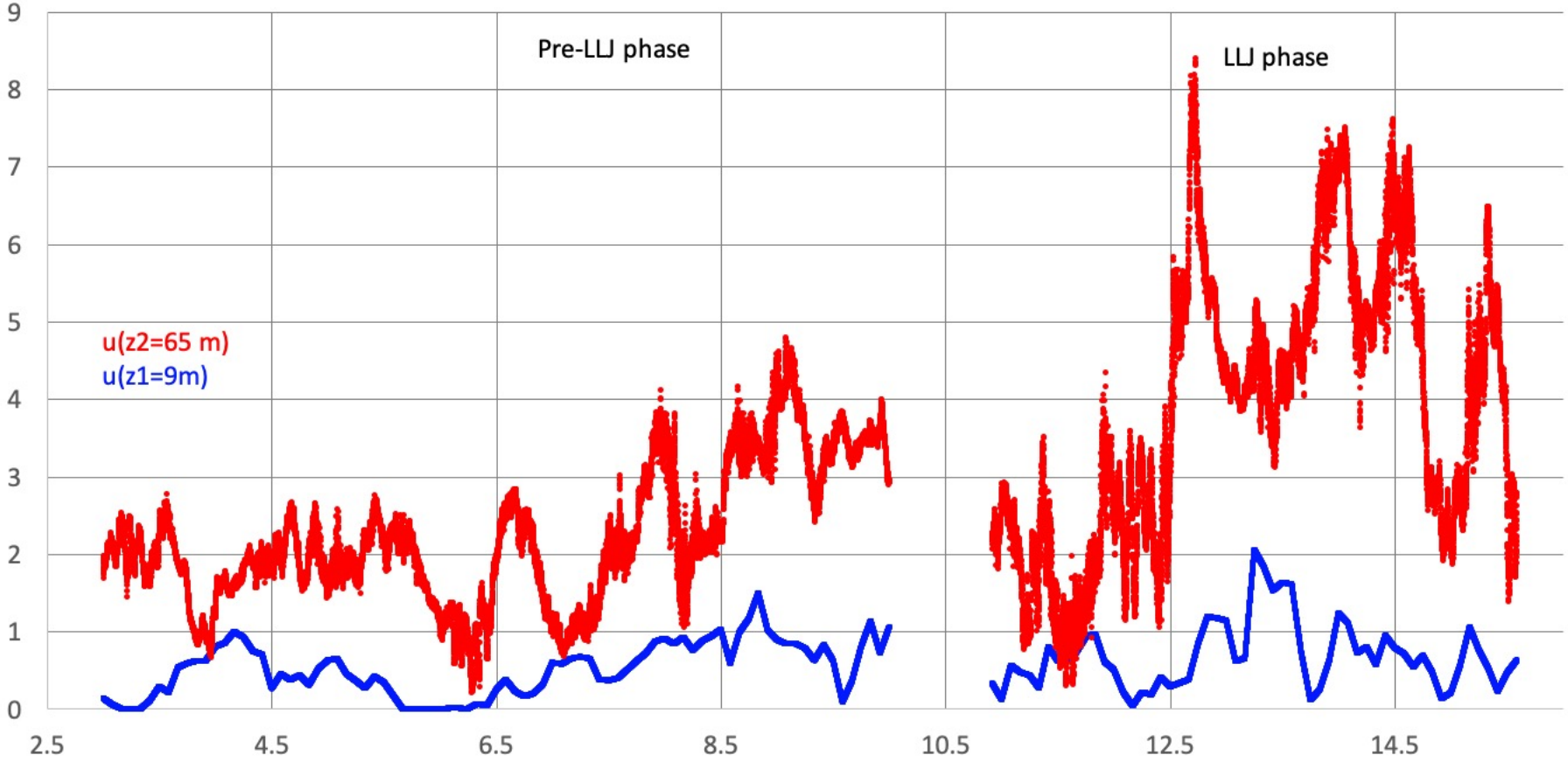

Figure 2: Time series of the observed wind velocity $u_h(z)$ (in units of $\mathrm{m\,s^{-1}}$) at $z_1 = 9\,\mathrm{m}$ and $z_2 = 65\,\mathrm{m}$. The abscissa shows the local time (LT) in hours.

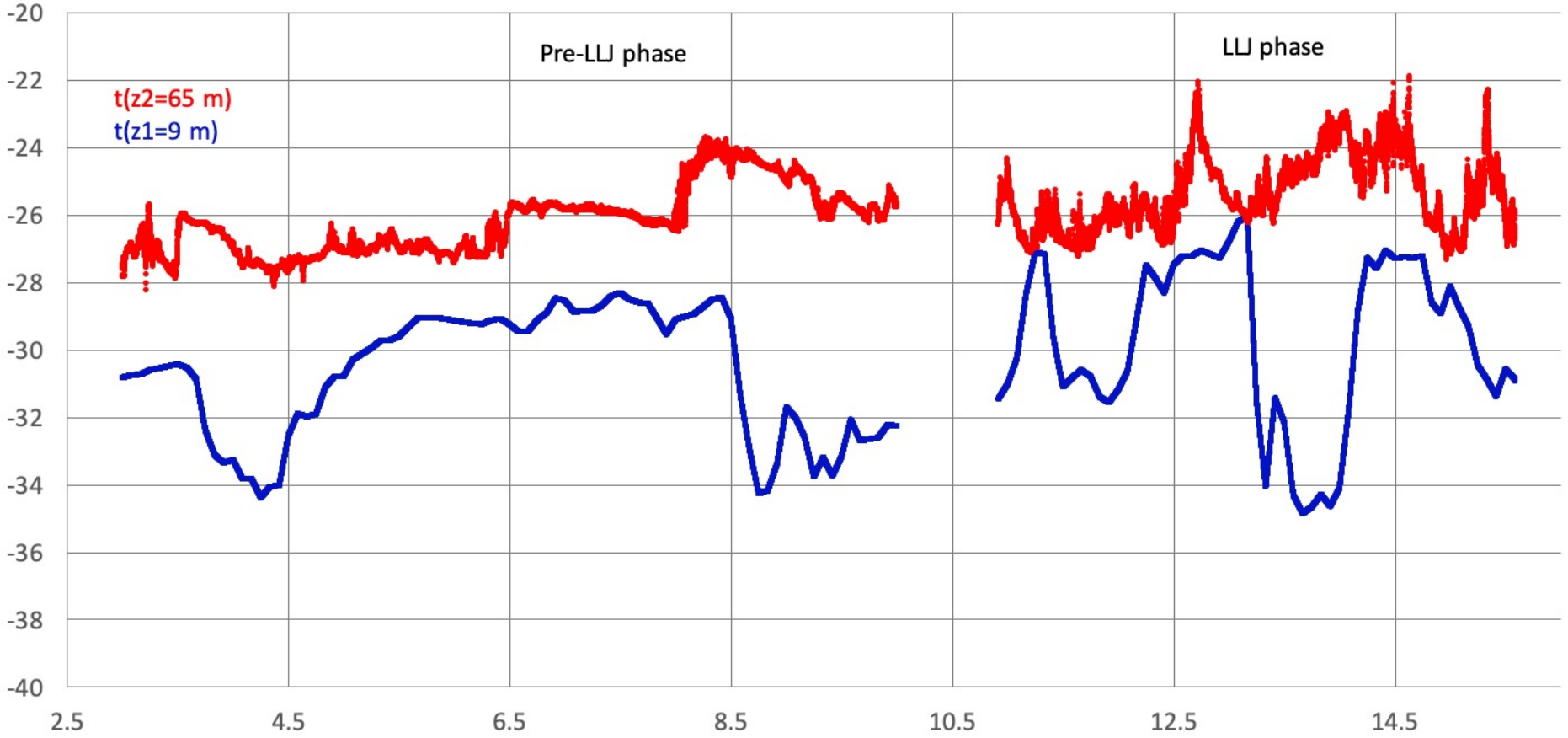

Figure 3: Time series of the observed temperature $\vartheta(z)$ (in units of °C) at $z_1 = 9\,\mathrm{m}$ and $z_2 = 65\,\mathrm{m}$. The abscissa shows the local time (LT) in hours.

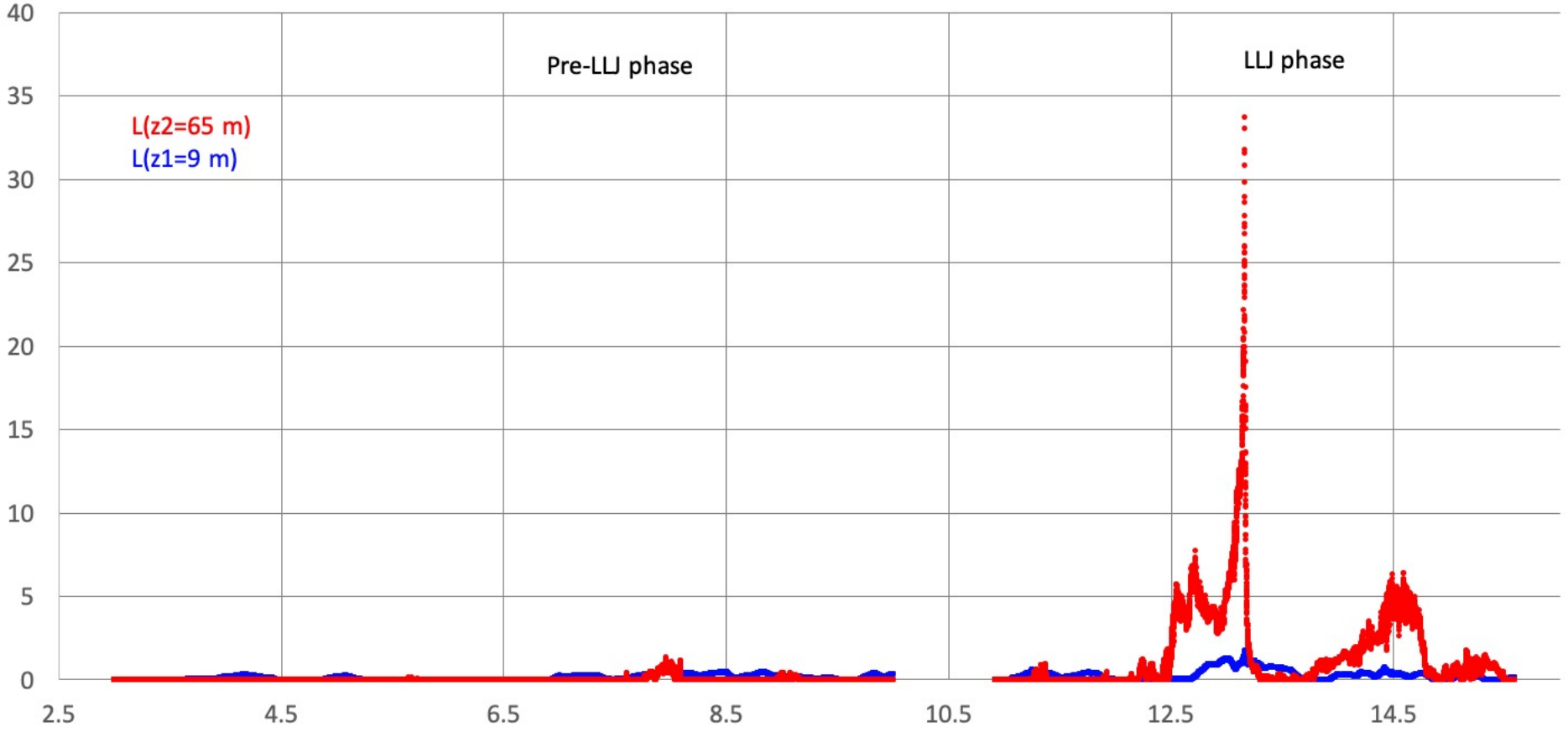

Figure 4: Time series of the calculated Monin-Obuchov length L (in units of m) at $z_1 = 9\,\mathrm{m}$ and $z_2 = 65\,\mathrm{m}$. The abscissa shows the local time (LT) in hours.

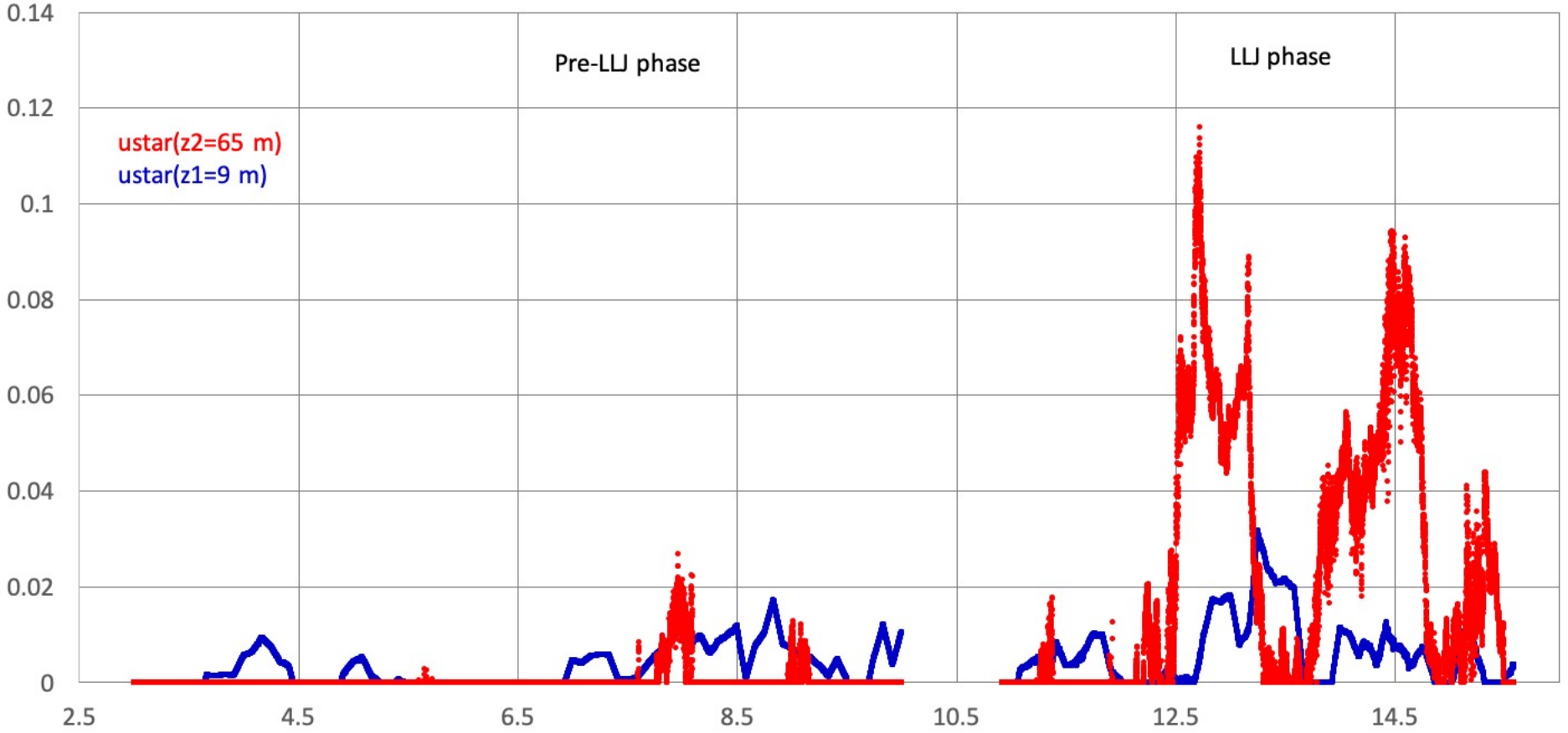

Figure 5: Time series of the friction velocity $u_\star$ (in units of $\mathrm{m\,s^{-1}}$) at $z_1 = 9\,\mathrm{m}$ and $z_2 = 65\,\mathrm{m}$. The abscissa shows the local time (LT) in hours.

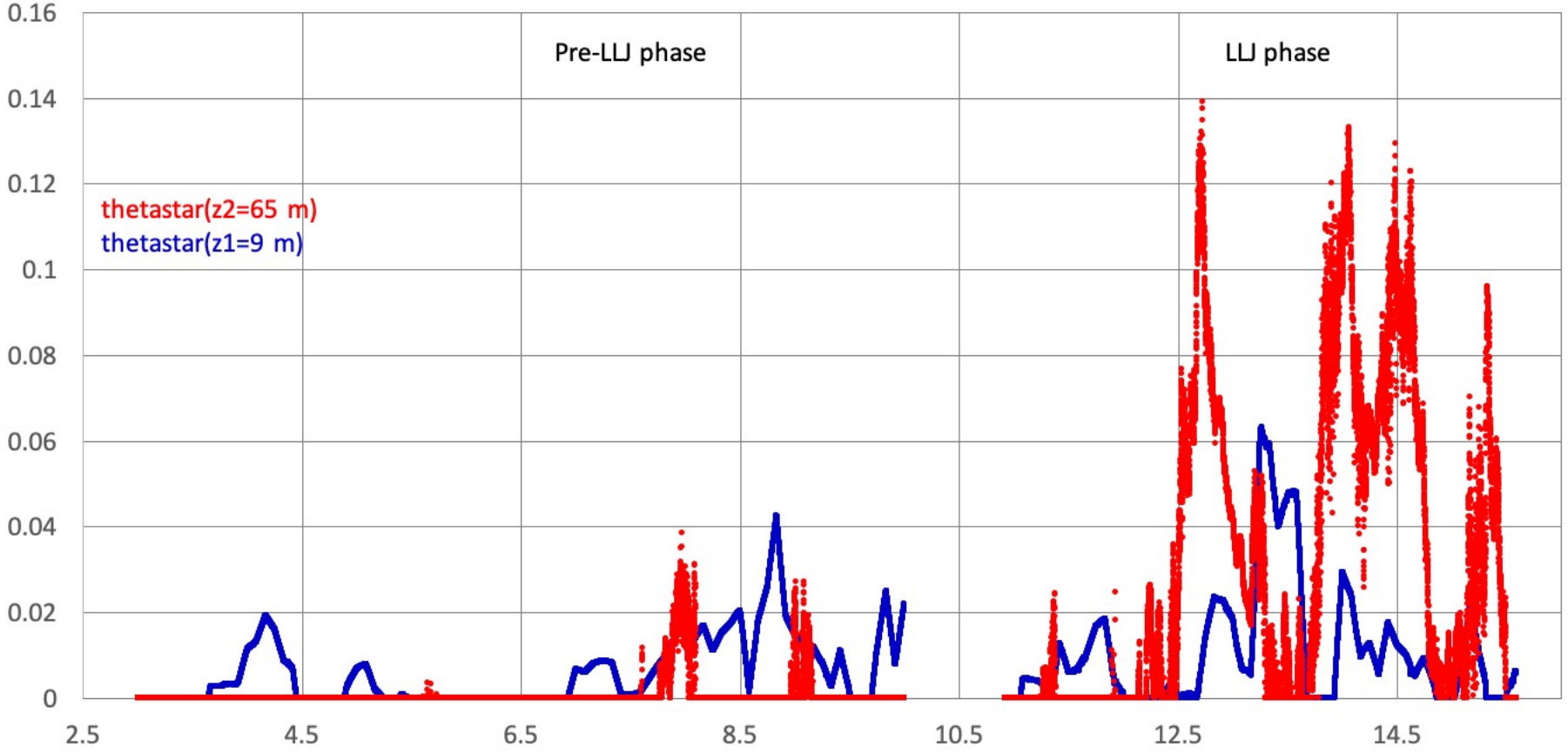

Figure 6: Time series of the kinematic scaling temperature $\theta_\star$ (in units of K) at $z_1 = 9\,\mathrm{m}$ and $z_2 = 65\,\mathrm{m}$. The abscissa shows the local time (LT) in hours.

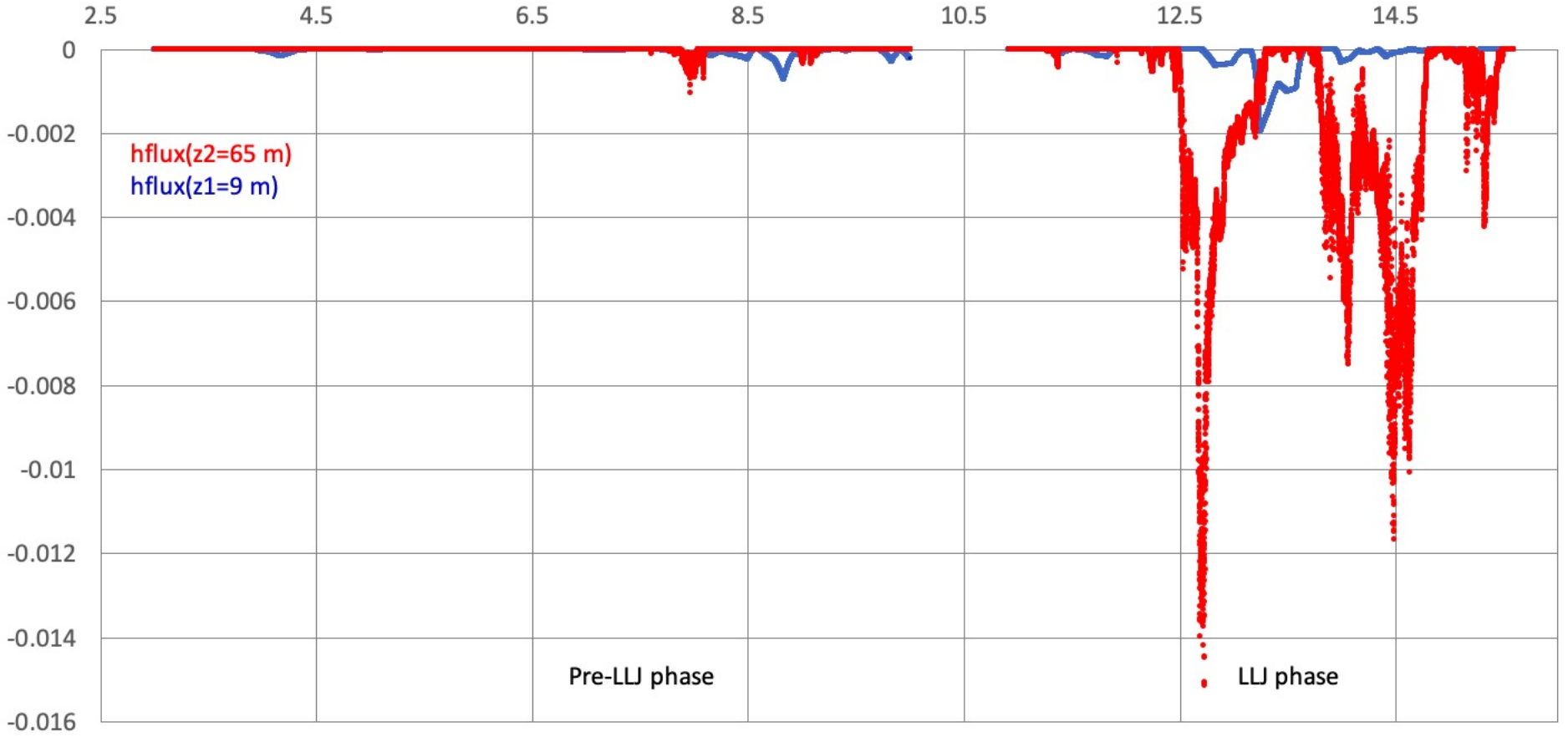

Figure 7: Time series of the kinematic heat flux $\overline{w'\theta'}$ (in units of $\mathrm{K\,m\,s^{-1}}$) at $z_1 = 9\,\mathrm{m}$ and $z_2 = 65\,\mathrm{m}$. The abscissa shows the local time (LT) in hours.

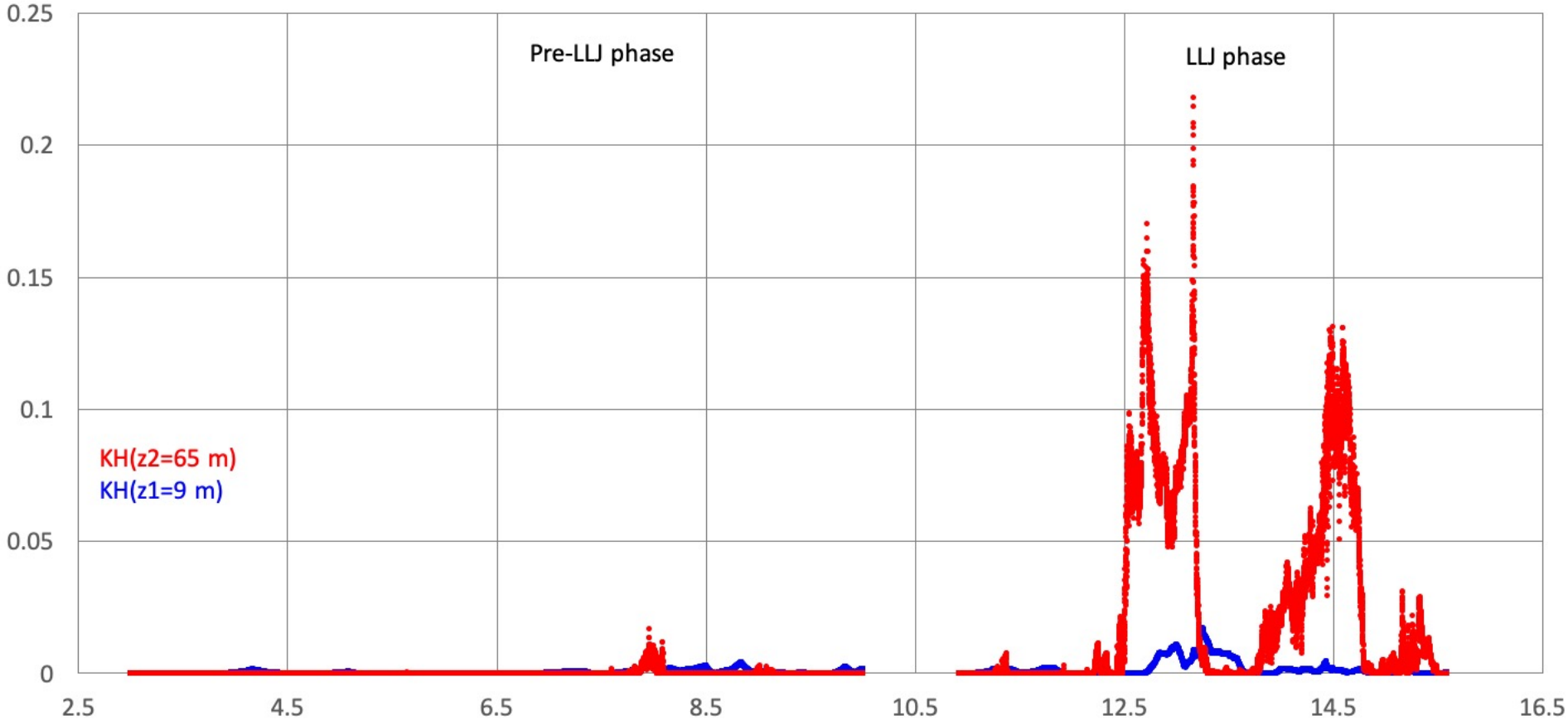

Figure 8: Time series of the eddy diffusivity of heat K_H (in units of $\mathrm{m^2\,s^{-1}}$) at $z_1 = 9\,\mathrm{m}$ and $z_2 = 65\,\mathrm{m}$. The abscissa shows the local time (LT) in hours.

Table 1: Time-averaged values and standard deviations of the Monin-Obuchov length scale L, the friction velocity $u_\star$, the kinematic temperature scale $\theta_\star$, the kinematic heat flux $\overline{w'\theta'}$, and the eddy diffusivity of heat K_H during the pre-LLJ and LLJ phases at $z_0 = 0.01\,\mathrm{m}$.

Pre-LLJ phase: 03:00:00 - 10:00:00 LT		
Height	$\langle L\rangle/\mathrm{m}$	σ_L/m
z_1	0.12	0.14
z_2	$2.3\cdot10^{-2}$	0.11
Height	$\langle u_\star\rangle/(\mathrm{m\,s^{-1}})$	$\sigma_{u_\star}/(\mathrm{m\,s^{-1}})$
z_1	$3.2\cdot10^{-3}$	0.18
z_2	$5.1\cdot10^{-4}$	0.11
Height	$\langle\theta_\star\rangle/\mathrm{K}$	σ_θ/K
z_1	$6.1\cdot10^{-3}$	$7.7\cdot10^{-3}$
z_2	$8.1\cdot10^{-4}$	$3.7\cdot10^{-3}$
Height	$\langle\overline{w'\theta'}\rangle/(\mathrm{K\,m\,s^{-1}})$	$\sigma_{\overline{w'\theta'}}/(\mathrm{K\,m\,s^{-1}})$
z_1	$-4.8\cdot10^{-5}$	$8.8\cdot10^{-5}$
z_2	$-9.1\cdot10^{-6}$	$5.3\cdot10^{-5}$
Height	$\langle K_H\rangle/(\mathrm{m^2\,s^{-1}})$	$\sigma_{K_H}/(\mathrm{m^2\,s^{-1}})$
z_1	$4.4\cdot10^{-4}$	$7\cdot10^{-4}$
z_2	$1.3\cdot10^{-4}$	$8.2\cdot10^{-4}$
LLJ phase: 10:55:00 - 15:35:12 LT		
Height	$\langle L\rangle/\mathrm{m}$	σ_L/m
z_1	0.29	0.32
z_2	1.54	2.6
Height	$\langle u_\star\rangle/(\mathrm{m\,s^{-1}})$	$\sigma_{u_\star}/(\mathrm{m\,s^{-1}})$
z_1	$6.3\cdot10^{-3}$	0.41
z_2	$2.3\cdot10^{-2}$	3
Height	$\langle\theta_\star\rangle/\mathrm{K}$	σ_θ/K
z_1	$1.1\cdot10^{-2}$	$1.4\cdot10^{-2}$
z_2	$3.1\cdot10^{-2}$	$3.6\cdot10^{-2}$
Height	$\langle\overline{w'\theta'}\rangle/(\mathrm{K\,m\,s^{-1}})$	$\sigma_{\overline{w'\theta'}}/(\mathrm{K\,m\,s^{-1}})$
z_1	$-1.6\cdot10^{-4}$	$3.3\cdot10^{-4}$
z_2	$-1.6\cdot10^{-3}$	$2.4\cdot10^{-3}$
Height	$\langle K_H\rangle/(\mathrm{m^2\,s^{-1}})$	$\sigma_{K_H}/(\mathrm{m^2\,s^{-1}})$
z_1	$1.8\cdot10^{-3}$	$3\cdot10^{-3}$
z_2	$2.4\cdot10^{-2}$	$3.7\cdot10^{-2}$

3 LLJ modelling approach

3.1 Previous works

One of the most popular theories to explain LLJs is those proposed by Blackadar (1957) describing the inertial oscillation of an inviscid flow without explicit inclusion of frictional stress. Based on this perception, Thorpe and Guymer (1977) developed a simple dynamic model allowing the investigation of the diurnal wind variation at appearance of a LLJ in the ABL. Beyrich and Klose (1987, 1990) advanced the approach of Thorpe and Guymer (1977) to predict the vertically averaged wind velocity in two ABL layers under LLJ conditions. For daytime conditions Beyrich and Klose (1987) assumed a single well-mixed layer extending from the surface to a height h_d, and for nighttime conditions the ABL was splitted into two layers: a lower, turbulent mixed layer extending from the surface to the height h_l, and an upper layer extending from the height h_l to the height h_u. Within these layers the wind is assumed to be independent of height and to represent mean conditions, implying a jump in the vertical wind profile at the layer boundaries. Momentum entrainment was considered by a prognostic equation for h_l at night, the momentum fluxes in the lower nocturnal ABL layer were parameterised in terms of the wind velocity and the dimensionless surface drag coefficient, and the horizontal advection terms of momentum were approximated by products of the precicted wind components and prescribed (fixed) values of the corresponding horizontal wind gradients. Within the framework of a conceptual study Beyrich and Klose (1987) analyzed the sensitivity of the LLJ intensity against momentum advection and vorticity. The authors found an increase (decrease) of the intensity of the wind maximum at positive (negative) momentum advection and anticyclonal (cyclonal) vorticity. A review of different LLJ models and a discussion of their pros and cons can be found in Shapiro and Fedorovich (2010).

Due to incomplete input information required for a realistic setup of the meteorological and orographic drivers affecting the observed LLJ phenomenon (e.g., the diurnal cycle of the momentum flux, momentum advection, vorticity, terrain-associated baroclinity) and for the purpose of a conceptual study of the impact of a LLJ on the horizontal transport of a passive tracer, in the present case a simple LLJ model proposed by Shapiro and Fedorovich (2010) will be used, which is based on Blackadar's inertial-oscillation theory and which has only three degrees of freedom. The required input parameters are empirically adjusted to the observed wind profiles.

3.2 The Shapiro-Fedorovich model

The Shapiro and Fedorovich (2010) solution describes the response of a frictional (ageostrophic) equilibrium (Ekman) flow to a sudden reduction of eddy diffusivity, i.e. the wind transition caused by a strong impulsive reduction of the post-sunset eddy diffusivity. The post-sunset eddy diffusivity has been introduced into the model to emulate the sudden reduction of the frictional stress after sunset. The model is based on the following assumptions:

- The flow is approximated by a one-dimensional homogeneous viscous incompressible pressure-driven Ekman flow over a horizontally homogeneous, flat terrain, i.e., the horizontal advection of momentum and vorticity effects are neglected.

- Momentum forcing originating from baroclinity is neglected.
- The PBL is dry.
- Far above the ground ($z \to \infty$) pressure gradient force and the Coriolis force are in geostrophic equilibrium resulting in a spatially and temporally constant geostrophic wind $\vec{v}_g = (v_{g,x}, v_{g,y})$.
- Near the surface the pressure gradient force, the Coriolis force, and the frictional force are in ageostrophic equilibrium. The frictional force is parameterized by a spatially constant eddy-viscosity term. The vertical eddy diffusivity of momentum is approximated by an "effective" value which is assumed to be constant in time and space (for motivation see **Appendix A**).
- The flow is located in a right-hand Cartesian coordinate system, in which the x-axis is aligned with the geostrophic wind vector, i.e., $v_{g,x} = v_g = |\vec{v}_g|$ and $v_{g,y} = 0$, and the y-axis cuts across isobars at right angles towards low pressure.

The governing equations describing the LLJ read (Shapiro and Fedorovich 2010, Eqs. (1) and (2) therein):

$$\frac{\partial v_x}{\partial t} = f v_y + K_M \frac{\partial^2 v_x}{\partial z^2} \ , \tag{10}$$

$$\frac{\partial v_y}{\partial t} = -f(v_x - v_g) + K_M \frac{\partial^2 v_y}{\partial z^2} \ . \tag{11}$$

Here, $v_g = v_{g,x} \equiv |\vec{v}_g|$ denotes the geostrophic wind speed, $v_x(z,t)$ and $v_y(z,t)$ are the wind components, K_M is the eddy diffusivity for momentum, and z is the height.

For $K_M = 0$ Eqs. (10) and (11) describe a harmonic inertial oscillation of an inviscid flow:

$$\frac{\partial^2 v_x}{\partial t^2} + f^2 v_x = f^2 v_g \ , \tag{12}$$

$$\frac{\partial^2 v_y}{\partial t^2} + f^2 v_y = 0 \ . \tag{13}$$

Here, $\omega = 2\pi/\tau = f$ denotes the angular frequency and $\tau = 2\pi/f$ the oscillation period, serving as the characteristic time scale of the LLJ. Introducing the dimensionless time $T_t = ft$, the oscillation period amounts $T_t = f\tau = 2\pi$.

3.3 Flow solutions involving friction

3.3.1 Steady state solution: Ekman helix

The boundary conditions comprise no-slip conditions at the ground level ($z = 0$) and pure geostrophic flow aloft ($z \to \infty$) (Shapiro and Fedorovich 2010, Eqs. (3) and (4) therein):

$$v_x(0,t) = 0 \ , \quad v_y(0,t) = 0 \ , \tag{14}$$

$$\lim_{z\to\infty} v_x(z,t) = v_g \ , \quad \lim_{z\to\infty} v_y(z,t) = 0 \ . \tag{15}$$

The initial state ($t = 0$) is defined by the sunset with the initial velocity components $v_{x,0}(z)$, $v_{y,0}(z)$ obtained as steady-state solutions of Eqs. (10) and (11) with eddy diffusivity $K_{M,0} > K_M$ (Shapiro and Fedorovich 2010, Eqs. (5) and (6) therein):

$$f v_{y,0} = -K_{M,0} \frac{\partial^2 v_{x,0}}{\partial z^2} \ , \tag{16}$$

$$f(v_{x,0} - v_g) = K_{M,0} \frac{\partial^2 v_{y,0}}{\partial z^2} \ . \tag{17}$$

The solutions are known as the Ekman Spiral (Stull 1997, Eq. (6.4.6c) therein):

$$v_{x,0}(z) = v_g \left[1 - \exp(-\gamma_E z)\cos(\gamma_E z)\right] \ , \quad \gamma_E = \sqrt{\frac{f}{2K_{M,0}}} \ , \tag{18}$$

$$v_{y,0}(z) = v_g \left[\exp(-\gamma_E z)\sin(\gamma_E z)\right] \ . \tag{19}$$

Here, the parameter γ_E is the inverse of the characteristic scale height of the Ekman layer.

3.3.2 Nonsteady-state solution: Shapiro-Fedorovich helix

For integration times $t \leq \tau/2 = \pi/f$ Shapiro and Fedorovich (2010, Eq. (7) therein) derived a solution of the nonsteady-state problem formulated in Eqs. (10) and (11) in non-dimensional variables (Shapiro and Fedorovich 2010, Eq. (7) therein):

$$\begin{aligned} V_x &\equiv \frac{v_x}{v_g} \ , \quad V_y \equiv \frac{v_y}{v_g} \ , \quad T_t \equiv f t \ , \\ Z &\equiv z\sqrt{\frac{f}{K_{M,0}}} \ , \quad k = \frac{K_M}{K_{M,0}} \ . \end{aligned} \tag{20}$$

Here, $K_{M,0}(> K_M)$ denotes the initial (sunset or pre-LLJ) eddy diffusivity and K_M the eddy diffusivity of the nocturnal stable ABL (LLJ phase). The analytical solution reads (Shapiro and Fedorovich 2010, Eqs. (35)–(37) therein):

$$\begin{aligned} V_x(Z,T_t) &= \sum_{n=0}^{\infty} \frac{I(Z,T_t;n)}{n!} \left\{ k^n \cos\left((1-k)T_t + \frac{n\pi}{2}\right) - \cos\left(\frac{n\pi}{2}\right) \right\} \\ &\quad + 1 - \exp\left(-\frac{Z}{\sqrt{2}}\right) \cos\left(\frac{Z}{\sqrt{2}} + (1-k)T_t\right) \ , \end{aligned} \tag{21}$$

$$\begin{aligned} V_y(Z,T_t) &= \sum_{n=0}^{\infty} \frac{I(Z,T_t;n)}{n!} \left\{ \sin\left(\frac{n\pi}{2}\right) - k^n \sin\left((1-k)T_t + \frac{n\pi}{2}\right) \right\} \\ &\quad + \exp\left(-\frac{Z}{\sqrt{2}}\right) \sin\left(\frac{Z}{\sqrt{2}} + (1-k)T_t\right) \ , \end{aligned} \tag{22}$$

$$I(Z,T_t;n) = \begin{cases} \operatorname{erfc}\left(\dfrac{Z}{2\sqrt{kT_t}}\right) & , \quad n = 0 \\ \dfrac{Z}{\sqrt{\pi k}} \dfrac{T_t^{n-1/2}}{2n-1} \exp\left(-\dfrac{Z^2}{4kT_t}\right) - \dfrac{Z^2}{2k} \dfrac{I(Z,T_t;n-1)}{2n-1} & , \quad n = 1,2,3,\ldots \end{cases} \tag{23}$$

In Eq. (23), $\mathrm{erfc}(x)$ denotes the complementary error function which is related to the error function $\mathrm{erf}(x)$ by the following equations:

$$\begin{aligned} \mathrm{erfc}(x) &= 1 - \mathrm{erf}(x) = \frac{2}{\sqrt{\pi}} \int_x^\infty \exp(-\xi^2)\,\mathrm{d}\xi \ , \\ \mathrm{erf}(x) &= \frac{2}{\sqrt{\pi}} \int_0^x \exp(-\xi^2)\,\mathrm{d}\xi \ . \end{aligned} \tag{24}$$

A highly accurate polynomial approximation of $\mathrm{erf}(x)$ with a maximal error of $1.2{\cdot}10^{-7}$ for any real argument is given by Press et al. (1996, p. 214 therein)[3]:

$$\begin{aligned} \mathrm{erf}(x) &= \begin{cases} 1-\tau & , \ x \geq 0 \ , \\ \tau - 1 & , \ x < 0 \ , \end{cases} \\ \tau &= \lambda \exp\big(-x^2 - 1.26551223 + 1.00002368\lambda + 0.37409196\lambda^2 \\ &\quad +0.09678418\lambda^3 - 0.18628806\lambda^4 + 0.27886807\lambda^5 - 1.13520398\lambda^6 \\ &\quad +1.48851587\lambda^7 - 0.82215223\lambda^8 + 0.17087277\lambda^9 \big) \ , \\ \lambda &= \frac{1}{1+0.5|x|} \ . \end{aligned} \tag{25}$$

The solution given by Eqs. (20)–(24) relies on approximations which restrict the applicability of the calculus to small non-dimensional times corresponding to half of an inertial oscillation period of $T_t = ft < \pi$. Adopting the eddy diffusivity in the daytime convective ABL (pre-LLJ phase) in the interval $K_{M,0} = (10 - 100)\,\mathrm{m^2\,s^{-1}}$ and in the stable nocturnal ABL (LLJ phase) in the interval $K_M = (0.01 - 1)\,\mathrm{m^2\,s^{-1}}$, the turbulence reduction parameter is expected to vary in the range $k = 0.0001 - 0.1$.

The correctness of the computer implementation of the calculus given by Eqs. (20)–(24) has been checked by comparing the simulated evolution of the vertical profiles V_x, V_y for $k = 0.1$ and $T_t \leq 2.5$ with the corresponding predictions by Shapiro and Fedorovich (2010, Fig. 2, left panel therein) (see **Figs. 9** and **10**).

3.4 Estimation of model input parameters

3.4.1 Model degrees of freedom

For given geographical latitude $\varphi = 80^\circ\,\mathrm{N}$ the Coriolis parameter amounts $f = 1.432 \cdot 10^{-4}\,\mathrm{s^{-1}}$. With this constraint the LLJ model described by Eqs. (20)–(24) has three degrees of freedom in form of the following scaling parameters:

1. the geostrophic wind speed $v_g = |\vec{v}_g|$,
2. the eddy diffusivity of momentum at pre-LLJ conditions, $K_{M,0}$, and
3. the turbulence reduction parameter $k = K_M/K_{M,0} < 1$, defined by the ratio of the eddy diffusivity of momentum during the LLJ phase, K_M, to those during the pre-LLJ phase, $K_{M,0}$.

[3]The special form the polynomial can be found in `https://en.wikipedia.org/wiki/Error_function`, accessed: 9 April 2021.

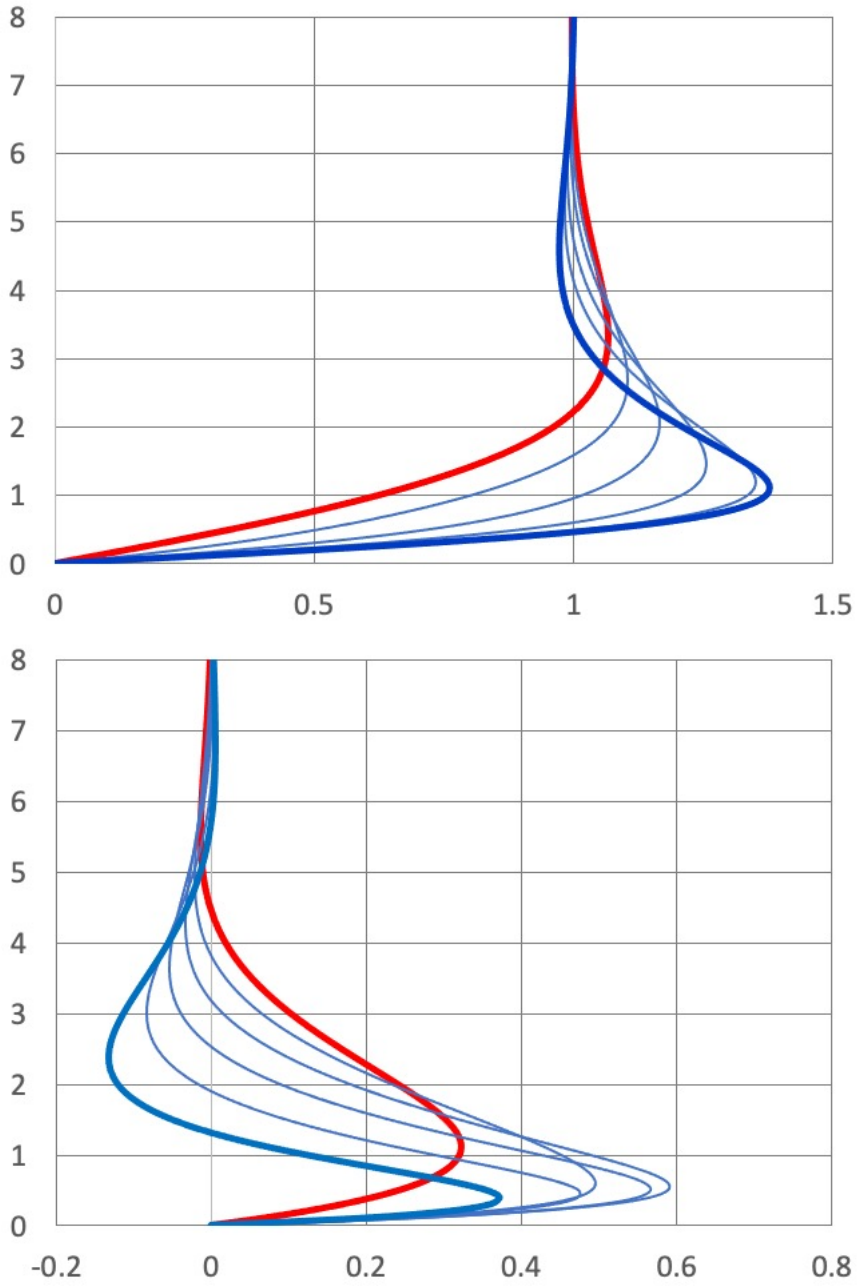

Figure 9: Evolution of vertical profiles of $V_x(Z, T_t)$ according to Eq. (21) (top panel) and of $V_y(Z, T_t)$ according to Eq. (22) (bottom panel) for $k = 0.1$ at dimensionless times $T_t = 0, 0.5, 1, 1.5, 2, 2.5$, respectively. The abscissa shows the dimensionless velocity components V_x and V_y and the ordinate the dimensionless height Z. The red graph corresponds to $T_t = 0$, the thick blue graph to $T_t = 2.5$. The figure corresponds to Shapiro and Fedorovich (2010, Fig. 2, left-top and left-bottom panels therein).

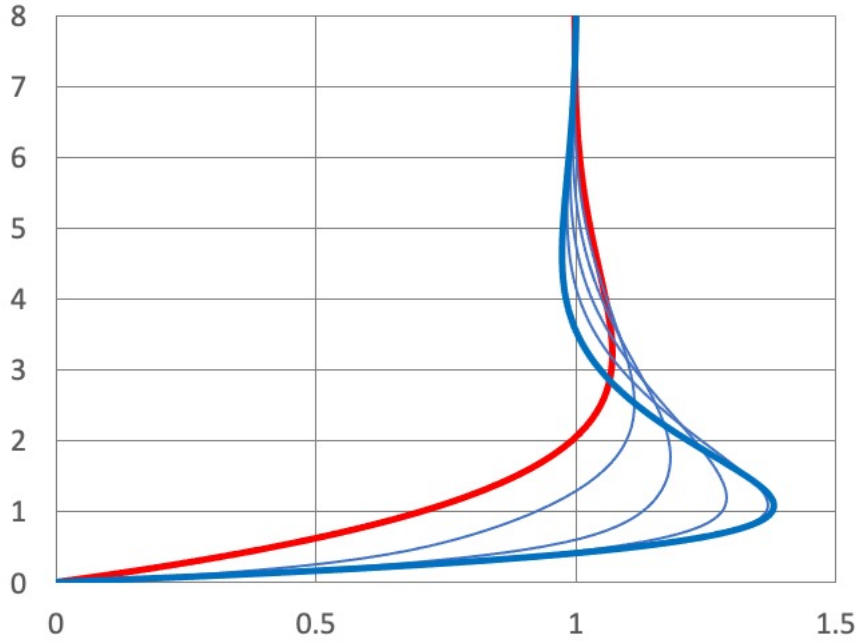

Figure 10: Evolution of vertical profile of the horizontal wind velocity $V = \sqrt{V_x^2 + V_y^2}$ for $k = 0.1$ at dimensionless times $T_t = 0, 0.5, 1, 1.5, 2, 2.5$, respectively. The abscissa shows the dimensionless wind velocity V and the ordinate the dimensionless height Z. The red graph corresponds to $T_t = 0$, the thick blue graph to $T_t = 2.5$.

3.4.2 Definition of the cost function

Owing to the lack of corresponding observations, the three unknown parameters $v_g = |\vec{v}_g|$, $K_{M,0}$, and k are empirically adjusted to ensure a minimum of the relative deviation of the simulated LLJ profile from the observed LLJ one. This is achieved by minimization of the following cost function χ^2 (in units of $\mathrm{m\,s^{-1}}$):

$$\chi^2 = \frac{1}{z_2 - z_1} \int_{z_1}^{z_2} \frac{\left(v_{h,sim}(z') - \overline{v}_{h,obs}(z')\right)^2}{\overline{v}_{h,obs}(z')} \,\mathrm{d}z' \approx \frac{1}{K} \sum_{k=1}^{K} \frac{\left(v_{h,sim}(z_k) - \overline{v}_{h,obs}(z_k)\right)^2}{\overline{v}_{h,obs}(z_k)} \,. \tag{26}$$

Here, the quantity $v_{h,sim}(z,t)$ denotes the actual value of the simulated horizontal wind velocity, and $\overline{v}_{h,obs}(z)$ is the mean vertical profil of the observed horizontal wind velocity during the LLJ phase. The index $k = 1, \ldots, K$ specifies the vertical levels of the observations.

The mean horizontal wind during the LLJ phase, $\overline{v}_{h,obs}(z)$, was derived from the wind measurements conducted on March 29, 2018, at Villum. The LLJ phase was assigned to the time period from $t_1 = 10{:}55{:}00\,\mathrm{LT}$ to $t_2 = 15{:}35{:}12\,\mathrm{LT}$, corresponding to a duration or averaging time of $\Delta t_{av} = t_2 - t_1 = 16,812\,\mathrm{s}$. **Table 2** shows the averaged normalized horizontal wind velocity, $\overline{v}_{h,n}(\overline{\zeta})$, as a function of the averaged normalized height, $\overline{\zeta} =$

$\overline{z/z_{inv}(t)}$, according to the following averaging rule:

$$\overline{v}_{h,n}(\overline{\zeta}) = \overline{\left(\frac{v_{h,obs}}{u_{h,max}}\right)} = \frac{1}{\Delta t_{av}} \int_{t_1}^{t_2} \left(\frac{v_{h,obs}(\zeta(t),t)}{v_{h,max}(t)}\right) \, \mathrm{d}t \; . \tag{27}$$

Table 2: Normalized observation height, $\overline{\zeta} = \overline{(z/z_{inv})}$, and normalized horizontal wind velocity, $\overline{v}_{h,n} = \overline{(v_{h,obs}/v_{h,max})}$, averaged over the LLJ phase on March 29, 2018, at Villum, lasting from $t_1 = 10{:}55{:}00\,\mathrm{LT}$ to $t_2 = 15{:}35{:}12\,\mathrm{LT}$, corresponding to a duration or averaging time of $\Delta t_{av} = t_2 - t_1 = 16,812\,\mathrm{s}$.

$\overline{\zeta}$	$\overline{v}_{h,n}$	$\overline{\zeta}$	$\overline{v}_{h,n}$	$\overline{\zeta}$	$\overline{v}_{h,n}$	$\overline{\zeta}$	$\overline{v}_{h,n}$
0.0	0.189	1.0	0.901	2.0	0.55	3.0	0.645
0.1	0.203	1.1	0.913	2.1	0.555	3.1	0.658
0.2	0.238	1.2	0.878	2.2	0.556		
0.3	0.252	1.3	0.832	2.3	0.575		
0.4	0.269	1.4	0.750	2.4	0.563		
0.5	0.323	1.5	0.683	2.5	0.573		
0.6	0.426	1.6	0.618	2.6	0.587		
0.7	0.534	1.7	0.564	2.7	0.611		
0.8	0.624	1.8	0.559	2.8	0.623		
0.9	0.771	1.9	0.557	2.9	0.64		

For the evaluation of Eq. (26) it appeared useful to represent the table values of the normalized wind profile (presented in **Table 2**) in form of a polynomial with the corresponding fitting coefficients given in **Table 3**:

$$\overline{v}_{h,n}(\overline{\zeta}) \approx \sum_{k=1}^{16} a_k \overline{\zeta}^{k-1} \; . \tag{28}$$

Table 3: Fitting coefficients a_k, $k = 1, \ldots, 16$ in Eq. (28).

k	a_k	k	a_k
1	0.18690541555635	9	14.4518926063945
2	0.112329796068606	10	−1.16942204556484
3	1.81179299601583	11	−12.5137465190373
4	−8.82860373971508	12	11.4064845465657
5	13.1297909896452	13	−4.89610126318892
6	4.5336996274696	14	1.16811862995693
7	−17.0126607348389	15	−0.149847272642797
8	−1.37074014755486	16	0.00810521684840272

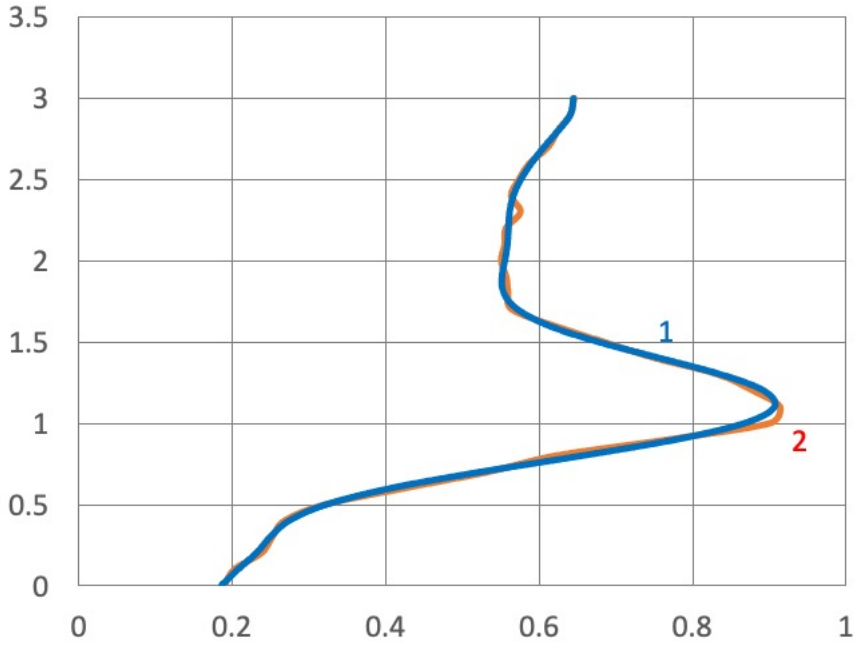

Figure 11: Vertical profile of the time-averaged normalized horizontal wind velocity $\overline{v}_{h,n}(\zeta)$ during the LLJ phase from the polynomial approximation according to Eq. (28) (graph 1, blue) in comparison to the observations (graph 2, red). The abscissa shows the normalized horizontal wind velocity $\overline{v}_{h,n}(\zeta)$, the ordinate the normalized height $\overline{\zeta} = \overline{z/z_{inv}(t)}$.

Table 4: Inversion height, z_{inv}, and the maximum of the horizontal wind velocity, $v_{h,max}$, observed during the LLJ phase on March 29, 2018, at Villum. The LLJ duration time amounts $\Delta t_{av} = 16,812\,\mathrm{s}$.

Local time (LT)	z_{inv}/m	$v_{h,max}/\mathrm{m\,s^{-1}}$
10 : 55 : 00	115.0	6.6
11 : 25 : 00	128.0	7.3
12 : 08 : 20	128.0	7.9
12 : 34 : 22	123.0	7.6
13 : 36 : 52	123.0	9.7
14 : 15 : 47	92.0	8.0
14 : 59 : 09	110.0	6.8
15 : 35 : 12	124.0	8.2
Mean value	117.88	7.77
Standard deviation	11.37	0.89

Figure 11 shows the vertical profile of the normalized horizontal wind velocity, $\overline{v}_{h,n}(\overline{\zeta})$, averaged over the observation interval Δt_{av}. The absolute amount of the relative deviation (i.e., the misfit) of the polynomial given by Eq. (28) from the observed profile $\overline{v}_{h,n,obs}(\overline{\zeta})$ does not exceed a value of $5.5\,\%$ in the interval $0 \leq \overline{\zeta} \leq 3.1$. One can conclude that Eq. (28) (blue graph in **Figure 11**) provides a sufficiently good approximation of the observed normalized wind profile.

The mean observed wind velocity as function of the altitude, $\overline{v}_{h,obs}(z)$, can be determined from Eq. (28) via Eq. (29) if certain constraints regarding the time variations of $v_{h,obs}(t)$ and $v_{h,max}(t)$ are fulfilled (see **Appendix B**):

$$\overline{v}_{h,obs}(z) \approx \underbrace{\overline{v}_{h,n}(\overline{\zeta})}_{\text{Eq.(28)}} \cdot \overline{v}_{h,max} \ , \quad \overline{\zeta} \approx \frac{z}{\overline{z}_{inv}} \tag{29}$$

The mean values of the inversion height, $\overline{z}_{inv}$, and the maximum of the observed horizontal wind velocity during the LLJ phase, $\overline{v}_{h,max}$, are given in **Table 4**.

3.4.3 Search strategy for minimizing the cost function

With $\overline{u}_{h,obs}(z)$ given by Eq. (29), the cost function introduced by Eq. (26) can be evaluated. The parameters $\{u_g, K_{M,0}, k\}$ are varied until χ^2 (Eq. (26)) attains its minimum. This criterion ensures that the simulated LLJ wind fits best the mean observed LLJ wind, $\overline{u}_{h,obs}(z)$. The three parameters were varied independently with subsequently decreasing search intervals and increments (see **Table 5**). The parameter combination ensuring an absolute minimum of χ^2 across the sampled parameter space is presented in the last column of this table.

3.5 Simulated LLJ evolution

3.5.1 Estimation of the eddy diffusivities of momentum and heat

Starting the LLJ simulation at a simulation time of $t_s = 0\,\mathrm{s}$ with the minimum-cost parameters for the fine resolved window presented in **Table 5**, the χ^2 minimum was achieved at $t_{s,\chi^2_{min}} = 21,720\,\mathrm{s}$ corresponding to $T_t = ft = 3.1337 < \pi$. With $K_{M,0} = 3.7\,\mathrm{m^2\,s^{-1}}$ and $k = 0.098$ one obtains by virtue of $k = K_M/K_{M,0}$ the eddy diffusivity of momentum during the LLJ phase as $K_M = kK_{M,0} \approx 0.36\,\mathrm{m^2\,s^{-1}}$.

The determination of the turbulent heat flux in **Section 4.3** (Eq. (41)) and of the turbulent tracer flux in **Section 5.1** (Eq. (49)) requires the knowledge of the eddy diffusivity of heat, K_H, which is related to the eddy diffusivity of momentum, K_M, via the turbulent Prandtl number,

$$\mathrm{Pr}_t = \frac{K_M}{K_H} = \frac{\mathrm{Ri}_g}{\mathrm{Ri}_f} \ , \tag{30}$$

where Ri_g denotes the gradient Richardson number (Stull 1997, Eq. (5.6.2) therein)

$$\mathrm{Ri}_g(z) = \frac{\left(\frac{g}{\theta}\right)\frac{\partial \theta}{\partial z}}{\left(\frac{\partial v_x}{\partial z}\right)^2 + \left(\frac{\partial v_y}{\partial z}\right)^2} \ , \tag{31}$$

Table 5: Sampling intervals for parameter search and best parameter estimates

Search window	Parameter	Symbol	Unit	Range		Increment	Best estimate
				Min	Max		(at χ^2 minimum)
Coarse resolved	Time increment	Δt	s			60	
	Simulation time until χ^2 minimum	t_{s,χ^2}	s				$21,780$
	Cost function at minimum	χ^2_{min}	$\mathrm{m\,s^{-1}}$				0.1928
	Geostrophic wind	$\lvert\vec{u}_g\rvert$	$\mathrm{m\,s^{-1}}$	1.0	10.0	1.0	4.00
	Pre-LLJ eddy diffusivity for momentum	$K_{M,0}$	$\mathrm{m^2\,s^{-1}}$	1.0	5.0	1.0	4.00
	Turbulence reduction parameter	k	1	0.001	0.1	0.001	0.096
Medium resolved	Time increment	Δt	s			10	
	Simulation time until χ^2 minimum	t_{s,χ^2}	s				$21,310$
	Cost function at minimum	χ^2_{min}	$\mathrm{m\,s^{-1}}$				0.1916
	Geostrophic wind	$\lvert\vec{u}_g\rvert$	$\mathrm{m\,s^{-1}}$	3.5	4.5	0.1	3.90
	Pre-LLJ eddy diffusivity for momentum	$K_{M,0}$	$\mathrm{m^2\,s^{-1}}$	3.5	4.5	0.1	3.80
	Turbulence reduction parameter	k	1	0.08	0.1	0.001	0.095
Fine resolved	Time increment	Δt	s			5	
	Simulation time until χ^2 minimum	t_{s,χ^2}	s				$\mathbf{21,720}$
	Cost function at minimum	χ^2_{min}	$\mathrm{m\,s^{-1}}$				0.1915
	Geostrophic wind	$\lvert\vec{u}_g\rvert$	$\mathrm{m\,s^{-1}}$	3.8	4.0	0.05	$\mathbf{3.95}$
	Pre-LLJ eddy diffusivity for momentum	$K_{M,0}$	$\mathrm{m^2\,s^{-1}}$	3.6	3.9	0.05	$\mathbf{3.7}$
	Turbulence reduction parameter	k	1	0.094	0.099	0.001	$\mathbf{0.098}$

and Ri_f the flux Richardson number (Stull 1997, Eq. (5.6.1b) therein) [4],

$$\mathrm{Ri}_f(z) = \frac{\left(\frac{g}{\theta}\right)\overline{v_z'\theta'}}{\overline{v_z'v_x'}\frac{\partial v_x}{\partial z} + \overline{v_z'v_y'}\frac{\partial v_y}{\partial z}} \ . \tag{32}$$

For neutral stratification Stull (1997, Eq. (6.4.1c) therein) reported $\mathrm{Pr}_t \approx 0.75$. For a very stable nocturnal ABL over the Great Plains with $\mathrm{Ri}_g = 0.2$ and $\mathrm{Ri}_f = 0.08$ Lenschow et al. (1988) derived a value of $\mathrm{Pr}_t = \mathrm{Ri}_g/\mathrm{Ri}_f \approx 2.5$, which was found to be larger compared to Pr_t values from previous studies. Lenschow et al. (1988) hypothesized that this relatively large Prandtl number may be a result of the relatively rougher terrain encountered in their study. With reference to experimental data and numerical simulations, Li (2019, Fig. 6 therein) argued that under strongly stable conditions Pr_t is expected to increase nearly linearly with increasing Ri_g because at large Ri_g, Ri_f tends to saturate or level off towards its maximum value $\mathrm{Ri}_{f,max}$. From the referred plot of scattered data $\mathrm{Pr}_t/\mathrm{Pr}_{t,neutral}$ vs. Ri_g in Li (2019, Fig. 6 therein) one can tentatively derive by visual inspection $\mathrm{Pr}_t/\mathrm{Pr}_{t,neutral} \approx 1 \ldots 2$ at $\mathrm{Ri}_g \approx 0.2$. Considering the variation in the values $\mathrm{Pr}_{t,neutral}$ $(= 0.74 \ldots 1)$, and the scatter in the values $\mathrm{Pr}_t/\mathrm{Pr}_{t,neutral}$ reported by Li (2019, Fig. 6 therein), one arrives at $\mathrm{Pr}_t = 0.74 \ldots 2$. Hoewever, Li (2019,see references therein) referred to the elusiveness and ongoing debate regarding the behavior of Pr_t under stable conditions, especially when Pr_t is presented as a function of the stability parameter $\zeta = z/L$. There are studies which suggest Pr_t scattering around unity for $\zeta \leq 10$, others showing $\mathrm{Pr}_t \to 1$ as $\zeta \to \infty$, an very few predicting that Pr_t is not bounded by unity and continues to increase with ζ even as $\zeta \to \infty$. On the other hand, as Li (2019) argued, plots Pr_t against R_g derived from field and laboratory experiments and numerical simulations show Pr_t increasing with R_g. Grachev et al. (2007) demonstrated that the stability dependence of Pr_t depends on the choice of the independent variable: $\partial \mathrm{Pr}_t/\partial R_g > 0$ but $\partial \mathrm{Pr}_t/\partial \zeta < 0$ and $\partial \mathrm{Pr}_t/\partial R_f < 0$. Sorbjan and Grachev (2010) found Pr_t decreasing from 0.9 under near-neutral conditions to about 0.7 under very stable conditions. In view of the open questions concerning the stability dependence of the Prandtl number its numerical value is expectable in the range $0.7 \leq \mathrm{Pr}_t \leq 2.5$ under very stable conditions. With $K_M = 0.36\,\mathrm{m^2\,s^{-1}}$ obtained from the parameter adjustment (see **Table 5**) $K_H = K_M/\mathrm{Pr_t}$ is therefore expectable in the interval $0.144\,\mathrm{m^2\,s^{-1}} \leq K_H \leq 0.514\,\mathrm{m^2\,s^{-1}}$.

For the purpose of the present study a Prandtl number of $\mathrm{Pr}_t = 0.7$ resulting in $K_H = 0.514\,\mathrm{m^2\,s^{-1}}$ was used.

3.5.2 Comparison of the simulated and the observed LLJ wind profile

Figure 12 displays the vertical profile of the simulated horizontal wind velocity at the χ^2 minimum (achieved at $t_{s,\chi^2_{min}} = 21,720\,\mathrm{s}$, red graph) together with the observed horizontal wind velocity (in units of $\mathrm{m\,s^{-1}}$) during the LLJ phase averaged over the observation interval Δt_{av} (blue graph). The ordinate presents the height z (in units of m). While the location of the LLJ peak in the observed wind profile is well captured by the model, the

[4] The sign convention used in Eq. (32) according to (Stull 1997, p. 175 therein) differs from that used by Lenschow et al. (1988, Eqs. (12)–(13) therein). However, the experimental data reported in Lenschow et al. (1988, Table 1, Figs. 6 and 7 therein) are reconcilable with the sign convention in Eq. (32).

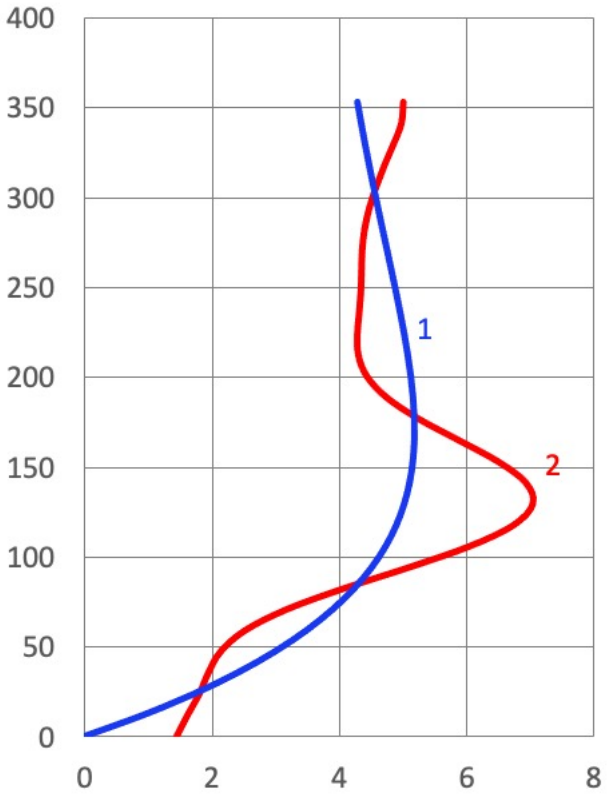

Figure 12: Vertical profile of the simulated horizontal wind velocity at the χ^2 minimum (achieved at $t_{s,\chi^2_{min}} = 21,720\,\mathrm{s}$ corresponding to $T_t = t_{s,\chi^2_{min}} f \approx 3.1337 \lesssim \pi$, graph 1, blue) for the parameter setup in **Table 5** ("fine resolved window") together with the observed horizontal wind velocity (in units of $\mathrm{m\,s^{-1}}$) during the LLJ phase (averaged over the observation interval Δt_{av}, graph 2, red, see **Fig. 11**). The abscissa shows the horizontal wind in units of $\mathrm{m\,s^{-1}}$, the ordinate the height z in units of m.

amplitude and width of the peak is not. The observed LLJ wind peak is more pronounced and narrower than the simulated one, which leads to a model underestimation of the slopes $\partial v(z)/\partial z$ (i.e., the wind shear) just below and above the altitude of the wind peak. This underprediction may be caused by the influence of the neglected acceleration terms in the momentum budget, such as (i) positive momentum advection and anticyclonal vorticity (Beyrich and Klose 1987) and/or (ii) the inclination of the Greenlandic ice sheet as a key orographic driver of katabatic winds (Heinemann 2004). The applied simplifications restrict the numerical simulations to a "trend prediction". However, despite this restriction the predictive power of the Shapiro-Fedorovich model is sufficiently high for its application within the framework of a conceptual study on the role of LLJs in aerosol transport (see **Section 5**).

In **Figure 13** the corresponding time evolution of the vertical profile of the simulated horizontal wind velocity (in units of $\mathrm{m\,s^{-1}}$) using parameter setup for the fine-resolved window in **Table 5** is presented at different integration times.

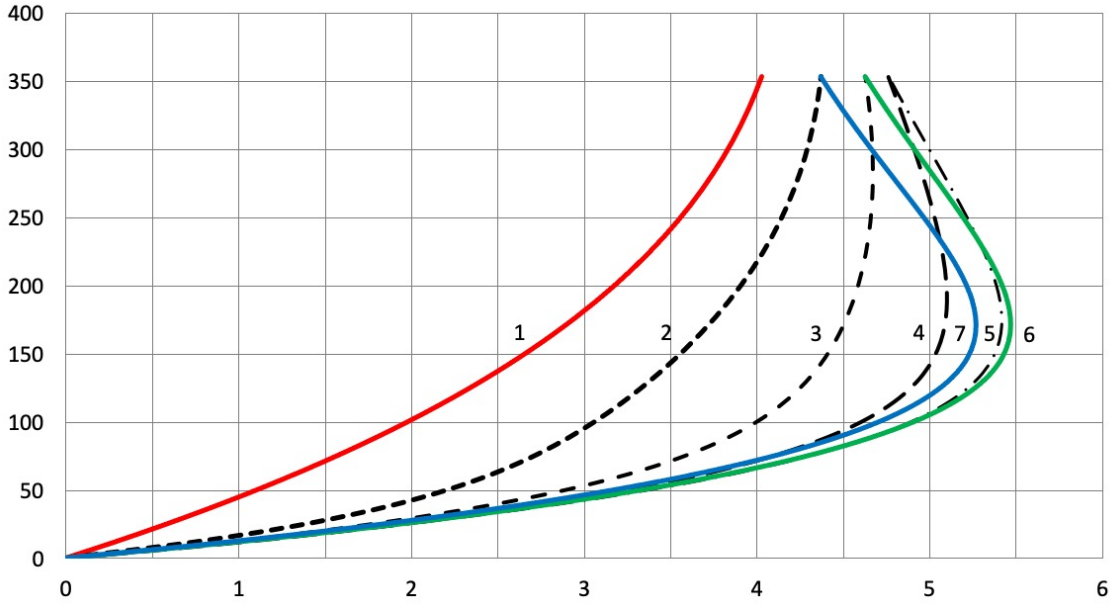

Figure 13: Time evolution of the vertical profiles of the simulated horizontal wind velocity (in units of $\mathrm{m\,s^{-1}}$) using parameter setup for the fine-resolved window in **Table 5**. The abscissa shows the horizontal wind velicity in units of $\mathrm{m\,s^{-1}}$, the ordinate the height z (in units of m). Graph 1-7: $T_t = 0\,(\text{red}),\ 0.5,\ 1.0,\ 1.5,\ 2.0,\ 2.5\,(\text{green}),\ 3.0\,(\text{blue})$ corresponding to simulation times of $t_s = 0\,(\text{red}),\ 3465,\ 6930,\ 10395,\ 13860,\ 17325\,(\text{green}),\ 20790\,\mathrm{s}\,(\text{blue})$.

4 Quantification of the contributions to the TKE budget during the LLJ phase

4.1 TKE balance equation

Based on the available measurements conducted during the LLJ phase observed during the PAMARCMiP field experiment 2018 an attempt is made to estimate the order of magnitude of the process contributions to the balance equation for the turbulent kinetic energy (TKE). Assuming horizontal homogeneity, the total time rate of change of TKE is controlled by four processes (Stull 1997, Eq. (6.5a) therein):

$$\frac{\partial e}{\partial t} = \left(\frac{\partial e}{\partial t}\right)_S + \left(\frac{\partial e}{\partial t}\right)_B + \left(\frac{\partial e}{\partial t}\right)_T + \left(\frac{\partial e}{\partial t}\right)_D , \tag{33}$$

$$
\begin{aligned}
\left(\frac{\partial e}{\partial t}\right)_S &= -\overline{v_x' v_z'}\frac{\partial v_x}{\partial z} - \overline{v_y' v_z'}\frac{\partial v_y}{\partial z} \ , \\
\left(\frac{\partial e}{\partial t}\right)_B &= \left(\frac{g}{\overline{\theta}}\right)\overline{v_z'\theta'} \ , \\
\left(\frac{\partial e}{\partial t}\right)_T &= -\frac{\partial}{\partial z}\left[\overline{v_z'\left(\frac{p'}{\varrho} + e'\right)}\right] \ , \\
\left(\frac{\partial e}{\partial t}\right)_D &= -\varepsilon \ .
\end{aligned}
\tag{34}
$$

The first term on the right-hand side (subscript S) of Eq. (33) describes the TKE production due to wind shear (mechanical turbulence), the second term (subscript B) the TKE production/loss due to buoyancy (TKE generation due to positive buoancy, TKE loss due to negative buoyancy), and the third term (subscript T) the TKE transport within the ABL, also known as redistribution term. This term is diffusive and vanishes when TKE is equally distributed thoughout the ABL. The redistribution term usually comprises also a contribution to the TKE balance originating from the work of pressure fluctuations, often associated with buoyancy or gravity waves. Finally, the fourth term (subscript D) describes the TKE loss by turbulence dissipation into heat. In the following, the contributions of these four terms to the TKE balance during the LLJ phase will be quantified. The results are based on a combination of wind- and temperature profiles measured during the LLJ phase of the PAMARCMiP field experiment and estimates of the eddy diffusivities for momentum and heat derived in **Section 3.4**.

4.2 Determination of the shear-induced TKE production

The shear-induced TKE production term is parameterized using the downgradient ansatz for the momentum fluxes,

$$
\overline{v_x' v_z'} = -K_M\frac{\partial v_x}{\partial z} \ , \quad \overline{v_y' v_z'} = -K_M\frac{\partial v_y}{\partial z} \ ,
$$

resulting in

$$
\left(\frac{\partial e}{\partial t}\right)_S = -\overline{v_x' v_z'}\frac{\partial v_x}{\partial z} - \overline{v_y' v_z'}\frac{\partial v_y}{\partial z} = K_M\left[\left(\frac{\partial v_x}{\partial z}\right)^2 + \left(\frac{\partial v_y}{\partial z}\right)^2\right] \ . \tag{35}
$$

With consideration of Eq. (20) and the gradients

$$
\begin{aligned}
\frac{\partial v_x}{\partial z} &= u_g\sqrt{\frac{f}{K_{M,0}}}\left(\frac{\partial V_x}{\partial Z}\right) \ , \\
\frac{\partial v_y}{\partial z} &= u_g\sqrt{\frac{f}{K_{M,0}}}\left(\frac{\partial V_y}{\partial Z}\right) \ ,
\end{aligned}
\tag{36}
$$

and by inserting Eq. (36) into (35) one arrives at the shear-induced TKE production:

$$
\left(\frac{\partial e}{\partial t}\right)_S = u_g^2 f\left(\frac{K_M}{K_{M,0}}\right)\left[\left(\frac{\partial V_x}{\partial Z}\right)^2 + \left(\frac{\partial V_y}{\partial Z}\right)^2\right] \ . \tag{37}
$$

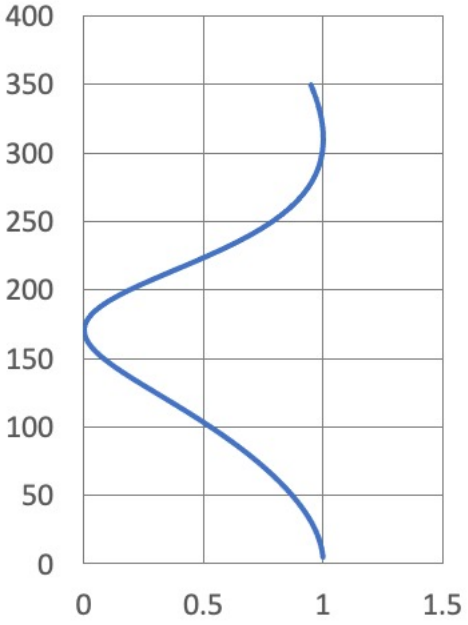

Figure 14: Vertical profile of the correction term $f_{\rm corr}$ according to Eq. (39) at the χ^2 minimum (achieved at $t_{s,\chi^2_{min}} = 21,720\,\mathrm{s}$ corresponding to $T_t = t_{s,\chi^2_{min}} f \approx 3.1337 \lesssim \pi$). The abscissa shows the dimensionless quantity $f_{\rm corr}$, the ordinate the height z in units of m.

The evaluation of $(\partial e/\partial t)_S$ requires the vertical profiles of both wind components, $v_x(z)$ and $v_y(z)$. At first, it has been checked, whether the sum term $(\partial v_x/\partial z)^2 + (\partial v_y/\partial z)^2$ in Eq. (37) can be approximated by $(\partial v/\partial z)^2$:

$$\left(\frac{\partial e}{\partial t}\right)_S \approx K_M \left(\frac{\partial v}{\partial z}\right)^2 = u_g^2 f \left(\frac{K_M}{K_{M,0}}\right) \left(\frac{\partial V}{\partial Z}\right)^2 , \quad V = \sqrt{V_x^2 + V_y^2} \, . \tag{38}$$

From the partial derivation of $v(z) = \sqrt{[v_x(z)]^2 + [v_y(z)]^2}$ with respect to z follows:

$$\begin{aligned} \left(\frac{\partial v}{\partial z}\right)^2 \;=\; & \left[\left(\frac{\partial v_x}{\partial z}\right)^2 + \left(\frac{\partial v_y}{\partial z}\right)^2\right] \\ & \times \underbrace{\left\{1 + \frac{2\left(v_x \dfrac{\partial v_x}{\partial z}\right)\left(v_y \dfrac{\partial v_y}{\partial z}\right) - \left[\left(v_y \dfrac{\partial v_x}{\partial z}\right)^2 + \left(v_x \dfrac{\partial v_x}{\partial z}\right)^2\right]}{\left(v \dfrac{\partial v_x}{\partial z}\right)^2 + \left(v \dfrac{\partial v_y}{\partial z}\right)^2}\right\}}_{= f_{\rm corr}} . \end{aligned} \tag{39}$$

Figure 14 displays the vertical profile of the correction term $f_{\rm corr}$ defined in Eq. (39) at the χ^2 minimum (achieved at $t_{s,\chi^2_{min}} = 21,720\,\mathrm{s}$ corresponding to $T_t = t_{s,\chi^2_{min}} f \approx 3.1337 \lesssim \pi$). The largest deviation of $f_{\rm corr}$ from unity is expectable at the LLJ level. As displayed in **Fig. 15**, however, the simulated shear-induced TKE production $(\partial e/\partial t)_S$ using Eq. (37)

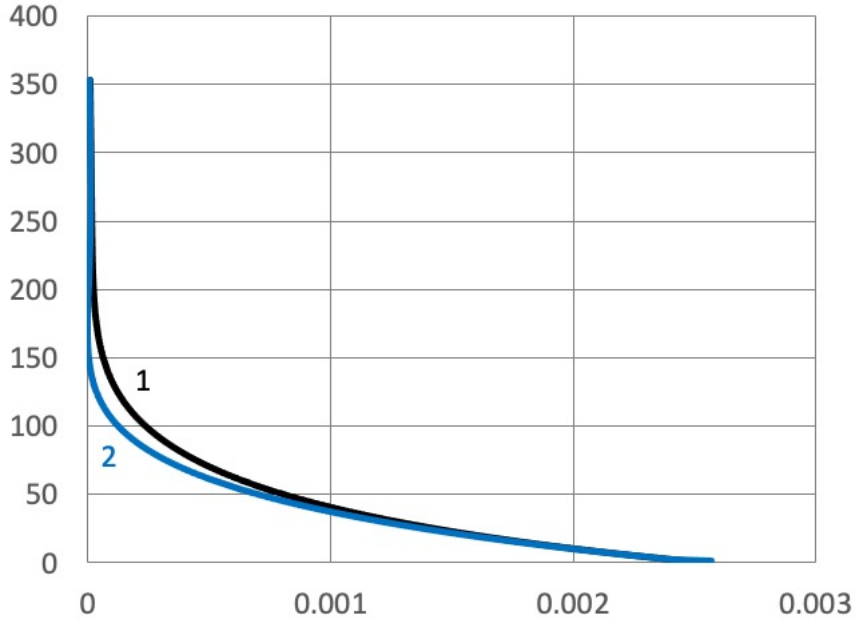

Figure 15: Vertical profiles of the simulated shear-induced TKE production, $(\partial e/\partial t)_S$ (in units of $\mathrm{m^2\,s^{-3}}$), according to Eq. (37) (graph 1, black) and according to the approximative form given by Eq. (38) (graph 2, blue) The abscissa shows $(\partial e/\partial t)_S$ in units of $\mathrm{m^2\,s^{-3}}$, the ordinate the height z in units of m.

(graph 1, black) is well reproduced by the approximative form using $v(z)$ according to Eq. (38) (graph 2, blue). Having confirmed the applicability of the $(\partial e/\partial t)_S$ approximation (38), now this equation will be evaluated using the observed horizontal wind speed given by Eqs. (28) and (29). The corresponding vertical gradient of the horizontal wind speed reads:

$$
\begin{aligned}
\frac{\partial \overline{v}_{h,obs}(z)}{\partial z} &\approx \left(\frac{\partial \overline{v}_{h,n}(\overline{\zeta})}{\partial \overline{\zeta}}\right)\left(\frac{\partial \overline{\zeta}}{\partial z}\right)\overline{v}_{h,max}\ , \quad \frac{\partial \overline{\zeta}}{\partial z} \approx \frac{1}{\overline{z}_{inv}}\ , \\
\frac{\partial \overline{v}_{h,n}(\overline{\zeta})}{\partial \overline{\zeta}} &\approx \sum_{k=1}^{16} a_k (k-1)\overline{\zeta}^{k-2} \\
\rightsquigarrow \quad \frac{\partial \overline{v}_{h,obs}(z)}{\partial z} &\approx \frac{\overline{v}_{h,max}}{\overline{z}_{inv}} \sum_{k=1}^{16} a_k (k-1)\overline{\zeta}^{k-2} = \frac{\overline{v}_{h,max}}{\overline{z}_{inv}} \sum_{k=2}^{16} a_k (k-1)\overline{\zeta}^{k-2} \\
\rightsquigarrow \quad \left(\frac{\partial e}{\partial t}\right)_S &\approx K_M \left(\frac{\overline{v}_{h,max}}{\overline{z}_{inv}} \sum_{k=2}^{16} a_k (k-1)\overline{\zeta}^{k-2}\right)^2 .
\end{aligned}
\tag{40}
$$

Figure 16 displays the vertical profiles of the simulated horizontal wind components, v_x (graph 1) and v_y (graph 2), and the corresponding horizontal wind speed, $v = \sqrt{v_x^2 + v_y^2}$ (graph 3), at the χ^2 minimum together with the observed horizontal wind velocity (in units of $\mathrm{m\,s^{-1}}$) during the LLJ phase (averaged over the observation interval Δt_{av}, graph 4, see **Fig. 11**). The simulated wind speed $v(z)$ (graph 3, green) is well rep-

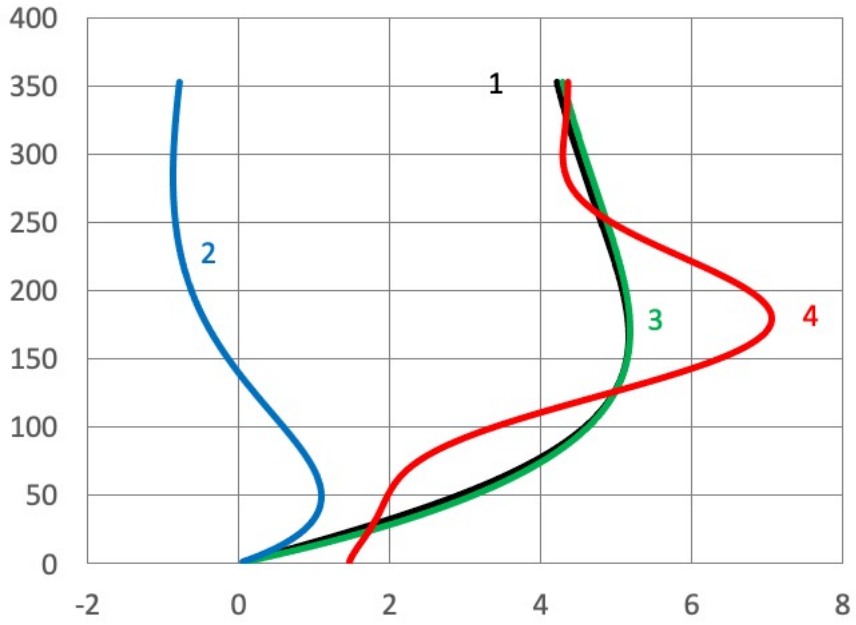

Figure 16: Vertical profiles of the simulated horizontal wind components, v_x (graph 1, black) and v_y (graph 2, blue), and the corresponding horizontal wind speed, $v = \sqrt{v_x^2 + v_y^2}$ (graph 3, green), at the χ^2 minimum (achieved at $t_{s,\chi^2_{min}} = 21,720\,\mathrm{s}$ corresponding to $T_t = t_{s,\chi^2_{min}} f \approx 3.1337 \lesssim \pi$) together with the observed horizontal wind velocity (in units of $\mathrm{m\,s^{-1}}$) during the LLJ phase (averaged over the observation interval Δt_{av} (graph 4, red, see **Fig. 11**). The abscissa shows the wind velocity in units of $\mathrm{m\,s^{-1}}$, the ordinate the height z in units of m.

resented by $v_x(z)$ (graph 1, black); the underestimation of the LLJ intensity by the model has already been discussed in **Section 3.5.2**.

Figure 17 shows the approximated shear-induced TKE production $(\partial e/\partial t)_S$ according to Eq. (38) using the simulated (graph 2, blue) and the observed $v(z)$ profile (graph 3, red). The model-based underestimation of the observed horizontal wind maximum (Eqs. (28) and (29), see **Fig. 12**) results in a remarkable difference in $(\partial e/\partial t)_S$ between the use of the simulated and the observed $v(z)$ profiles. As a consequence of the no-slip boundary condition at the ground level the simulated $v(z)$ reveals its largest vertical gradient at the ground which results in only one maximum of $(\partial e/\partial t)_S$ at the ground. In contrast to this, the observed $v(z)$ profile discloses three shear maxima, the primary one at $z \approx 125\,\mathrm{m}$ in the vicinity of the inversion height, a secondary one at $z \approx 225\,\mathrm{m}$, and a tertiary one close to the ground. The primary and secondary shear maxima in the observed $v(z)$ are a direct consequence of the more pronounced and narrower wind peak in the observed LLJ as compared to the simulated one (see discussion in **Section 3.5.2**). The three observed wind-shear maxima result in three corresponding $(\partial e/\partial t)_S$ maxima (see **Fig. 17**, graph 3, red). This result underpins the importance of the momentum advection, baroclinity, and orographic drivers of the katabatic wind for an appropriate prediction of the $(\partial e/\partial t)_S$ profile.

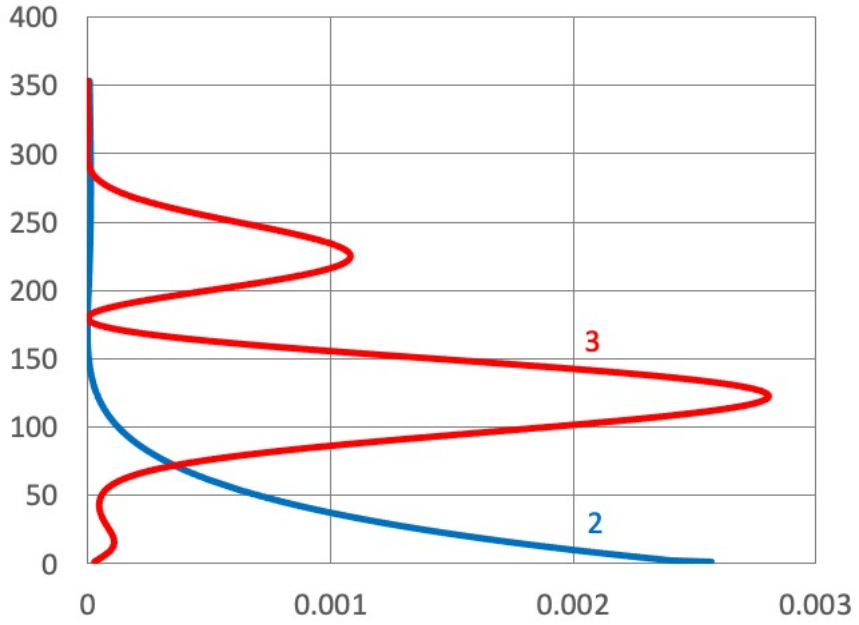

Figure 17: Vertical profiles of the simulated shear-induced TKE production, $(\partial e/\partial t)_S$ (in units of $\mathrm{m^2\,s^{-3}}$), according to the approximation (38) (graph 2, blue) together with the shear-induced TKE production derived on base of the observed, time-averaged horizontal wind velocity according to Eq. (40). The abscissa shows $(\partial e/\partial t)_S$ in units of $\mathrm{m^2\,s^{-3}}$, the ordinate the height z in units of m.

4.3 Determination of the buoyancy-induced TKE production/loss

The determination of the TKE change due to buoyancy, $(\partial e/\partial t)_B$ according to Eq. (33), requires the knowledge of the turbulent flux of sensible heat, $\overline{v_z'\theta'}$, which is estimated on the base of the classical downgradient ansatz (or small-eddy approximation) employing the observed vertical profile of the potential temperature averaged over the LLJ phase:

$$\overline{v_z'\theta'} \approx -K_H \frac{\partial \overline{\theta}_{obs}}{\partial z} \ . \tag{41}$$

Here, K_H denotes the eddy diffusivity of heat, and $\overline{\theta}_{obs}(z)$ the observed vertical profile of the potential temperature. The mean potential temperature during the LLJ phase, $\overline{\theta}_{obs}(z)$, was derived from the temperature measurements conducted on March 29, 2018, at Villum. The assignment of the LLJ phase was the same as for the wind velocity. **Table 6** shows the averaged normalized potential temperature, $\overline{\theta}_n(\overline{\zeta}) = \overline{\theta}(z)/\overline{\theta}_{inv}$, as a function of the averaged normalized height, $\overline{\zeta} = \overline{z/z_{inv}(t)}$, according to the following averaging rule:

$$\overline{\theta}_n(\overline{\zeta}) = \overline{\left(\frac{\theta_{obs}}{\theta_{inv}}\right)} = \frac{1}{\Delta t_{av}} \int_{t_1}^{t_2} \left(\frac{\theta_{obs}(\zeta(t),t)}{\theta_{inv}(t)}\right) \mathrm{d}t \ . \tag{42}$$

Here, θ_{inv} and z_{inv} denote the actual values of the potential temperature at the inversion and the inversion height.

Table 6: Normalized observation height, $\overline{\zeta} = \overline{(z/z_{inv})}$, and normalized potential temperature, $\overline{\theta}_n = \overline{(\theta_{obs}/\theta_{inv})}$ (with $\theta_{inv} = \theta_{obs}(z_{inv})$), averaged over the LLJ phase on March 29, 2018, at Villum, lasting from $t_1 = 10{:}55{:}00\,\mathrm{LT}$ to $t_2 = 15{:}35{:}12\,\mathrm{LT}$, corresponding to a duration or averaging time of $\Delta t_{av} = t_2 - t_1 = 16,812\,\mathrm{s}$.

$\overline{\zeta}$	$\overline{\theta}_n$	$\overline{\zeta}$	$\overline{\theta}_n$	$\overline{\zeta}$	$\overline{\theta}_n$	$\overline{\zeta}$	$\overline{\theta}_n$
0.0	0.9618	1.0	0.9996	2.0	1.0092	3.0	1.014
0.1	0.9677	1.1	1.0016	2.1	1.0100	3.1	1.0142
0.2	0.9739	1.2	1.0021	2.2	1.0108		
0.3	0.9769	1.3	1.0027	2.3	1.0115		
0.4	0.9790	1.4	1.0034	2.4	1.0122		
0.5	0.9818	1.5	1.0042	2.5	1.0127		
0.6	0.9851	1.6	1.0052	2.6	1.0131		
0.7	0.9879	1.7	1.0061	2.7	1.0133		
0.8	0.9908	1.8	1.007	2.8	1.0134		
0.9	0.9948	1.9	1.008	2.9	1.0139		

The vertical profile of the mean observed potential temperature, $\overline{\theta}_{obs}(z)$, can be determined to a good approximation from the normalized values $\overline{\theta}_{obs}(\overline{\zeta})$ given in **Table 6** (see **Appendix A**):

$$\overline{\theta}(z) \approx \overline{\theta}_n(\overline{\zeta}) \cdot \overline{\theta}_{inv} \ , \quad \overline{\zeta} \approx \frac{z}{\overline{z}_{inv}} \ . \tag{43}$$

Table 7: Inversion height, $z_{inv}(t)$, and potential temperature at the inversion height, $\theta_{inv} = \theta_{obs}(z_{inv})$, during the LLJ phase on March 29, 2018, at Villum. The averaging time amounts $\Delta t_{av} = 16,812\,\mathrm{s}$.

Local time (LT)	z_{inv}/m	θ_{inv}/K
$10:55:00$	115.0	251.12
$11:25:00$	128.0	253.48
$12:08:20$	128.0	252.85
$12:34:22$	123.0	252.99
$13:36:52$	123.0	252.84
$14:15:47$	92.0	253.00
$14:59:09$	110.0	251.89
$15:35:12$	124.0	252.10
Mean value	117.88	252.53
Standard deviation	11.37	0.72

The mean values of the inversion height, $\overline{z}_{inv}$, and the potential temperature at the inversion height during the LLJ phase, $\overline{\theta}_{inv}$, which enter Eq. (43) are given in **Table 7**.

Figure 18 shows the vertical profile of the time-averaged potential temperature during the LLJ phase, $\overline{\theta}(z)$ (in units of K) according to Eq. (43), which discloses a stable thermal stratification througout the whole PBL with two remarkable changes in the temperature lapse rate $\partial\overline{\theta}/\partial z$ at $z \approx 25\,\mathrm{m}$ and at the inversion height $z \approx 120\,\mathrm{m}$.

For the heat flux determination an eddy diffusivity of heat of $K_H \approx 0.514\,\mathrm{m^2\,s^{-1}}$ was used according to the discussion in **Section 3.5.1**. **Figure 19** shows the vertical profile of the approximated time-averaged kinematic heat flux during the LLJ phase, $\overline{v_z'\theta'}$ (in units of $\mathrm{K\,m\,s^{-1}}$) according to Eq. (41), which discloses a downward directed transport of sensible heat throughout the ABL with three distinct maxima: the primary occuring close to the surface at $z \approx 25\,\mathrm{m}$, the secondary one occurring at the inversion height $z \approx 120\,\mathrm{m}$, and a tertiary one at $z \approx 230\,\mathrm{m}$. These maxima in the downward directed heat fluxes lead to corresponding maxima in the (negative) buoyancy-induced TKE loss, $(\partial e/\partial t)_B = \left(g/\overline{\theta}\right)\overline{v_z'\theta'}$, as seen in **Fig. 20**. It should be mentioned that the quantity $\overline{v_z'\theta'}$ derived on the base of the time-averaged potential temperature $\overline{\theta}(z)$ is just as a proxy for the "true" time-averaged flux of sensible heat (due to nonlinearity effects on averaging, which are neglected here).

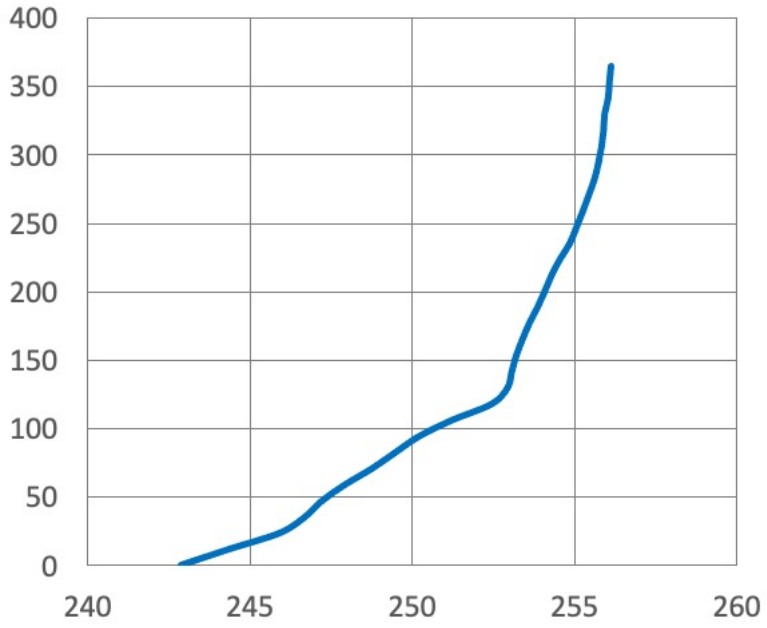

Figure 18: Vertical profile of the time-averaged potential temperature during the LLJ phase, $\overline{\theta}(z)$ according to Eq. (43). The abscissa shows $\overline{\theta}(z)$ in units of K, the ordinate the height level z in units of m.

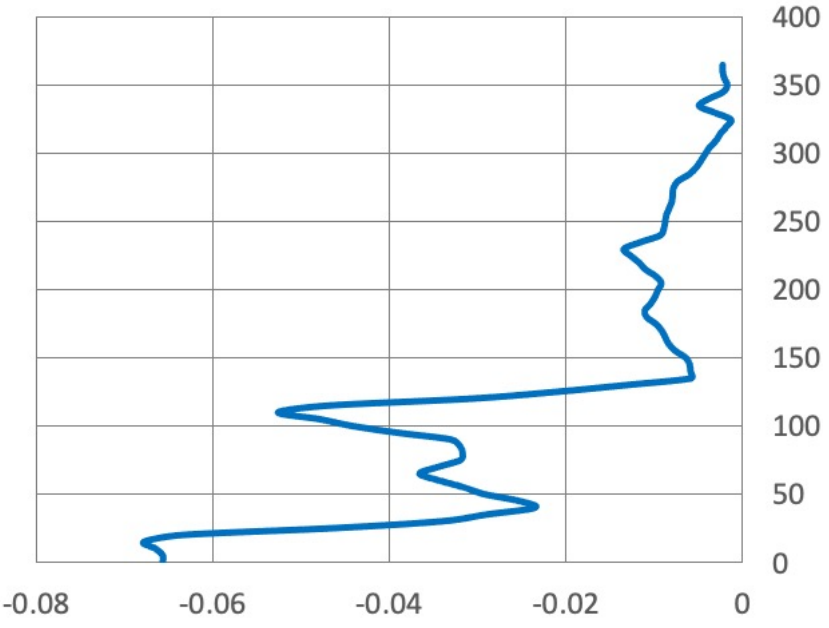

Figure 19: Vertical profile of the time-averaged kinematic flux of sensible heat, $\overline{v_z'\theta'} = -K_H\left(\partial\overline{\theta}/\partial z\right)$. The abscissa shows $\overline{v_z'\theta'}$ in units of $\mathrm{K\,m\,s^{-1}}$, the ordinate the height level z in units of m.

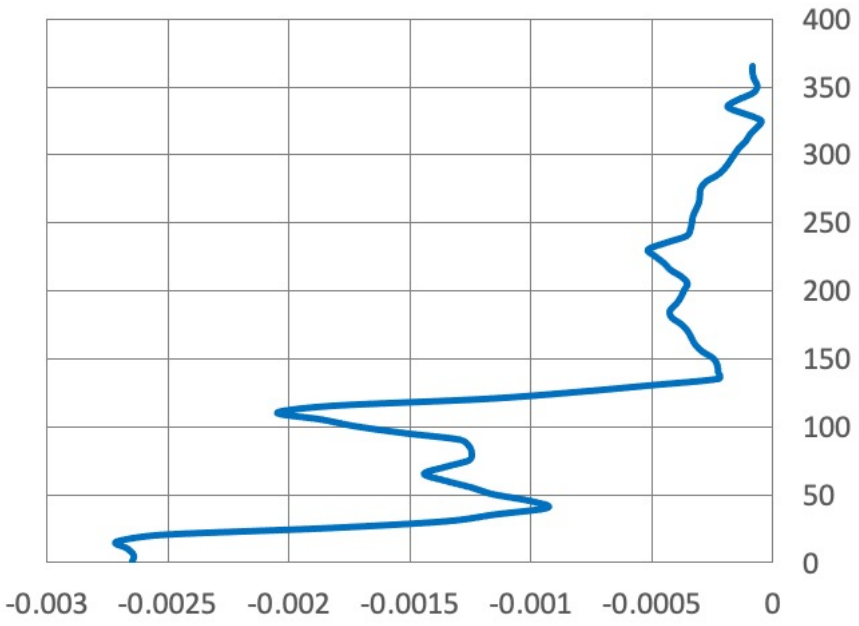

Figure 20: Vertical profile of the time-averaged buoyancy-induced TKE loss, $(\partial e/\partial t)_B = \left(g/\overline{\theta}\right) \overline{v_z' \theta'}$. The abscissa shows $(\partial e/\partial t)_B$ in units of $\mathrm{m}^2\,\mathrm{s}^{-3}$, the ordinate the height level z in units of m.

4.4 Determination of the TKE dissipation

Table 8 shows the table values of the normalized observation height, $\overline{\zeta} = \overline{(z/z_{inv})} \approx z/\overline{z}_{inv}$, and TKE dissipation rate, $\overline{\varepsilon}$ (in units of $\mathrm{m^2\,s^{-3}}$), averaged over the LLJ phase on March 29, 2018, at Villum, lasting from $t_1 = 10{:}55{:}00\,\mathrm{LT}$ to $t_2 = 15{:}35{:}12\,\mathrm{LT}$, corresponding to a duration or averaging time of $\Delta t_{av} = t_2 - t_1 = 16,812\,\mathrm{s}$. In **Fig. 21** the corresponding vertical profile is plotted. There are two distinct dissipation maxima: a primary one close to the surface at $z \approx 25\,\mathrm{m}$, and a secondary one above the inversion height at $z \approx 190\,\mathrm{m}$.

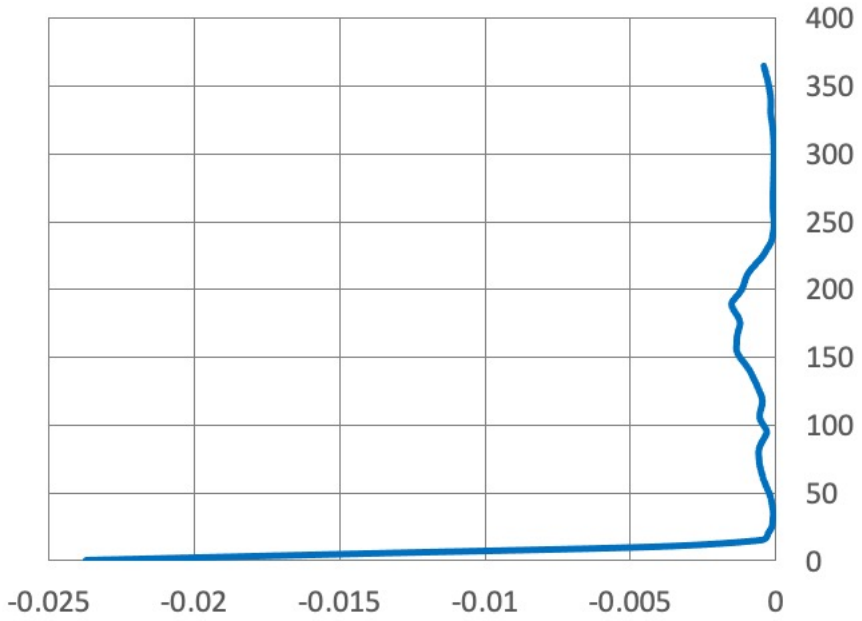

Figure 21: Vertical profile of the time-averaged TKE loss due to dissipation of turbulent kinetic energy into heat, $(\partial e/\partial t)_D = -\overline{\varepsilon}(z)$ according to Eq. (33), for the LLJ phase. The abscissa shows $(\partial e/\partial t)_D$ in units of $\mathrm{m^2\,s^{-3}}$, the ordinate the height level z in units of m.

4.5 Determination of the TKE redistribution

With neglect of the contribution of the work performed by pressure fluctuations, the TKE redistribution term in Eq. (33) approximately reads:

$$\left(\frac{\partial e}{\partial t}\right)_T \approx -\frac{\partial \overline{v_z' e'}}{\partial z} \,. \tag{44}$$

Parameterizing the turbulent TKE flux, $\overline{v_z' e'}$, using the small-eddy diffusivity approximation,

$$\overline{v_z' e'} = -K_M \frac{\partial e}{\partial z} \,, \tag{45}$$

and setting $K_M = \text{const.}$, one arrives at

$$\left(\frac{\partial e}{\partial t}\right)_T \approx K_M \frac{\partial^2 e}{\partial z^2} \,. \tag{46}$$

Table 8: Normalized observation height, $\overline{\zeta} = \overline{(z/z_{inv})}$, and TKE dissipation rate, $\overline{\varepsilon}$ (in units of $\mathrm{m^2\,s^{-3}}$), averaged over the LLJ phase on March 29, 2018, at Villum, lasting from $t_1 = 10{:}55{:}00\,\mathrm{LT}$ to $t_2 = 15{:}35{:}12\,\mathrm{LT}$, corresponding to a duration or averaging time of $\Delta t_{av} = t_2 - t_1 = 16,812\,\mathrm{s}$.

$\overline{\zeta}$	$\overline{\varepsilon}$	$\overline{\zeta}$	$\overline{\varepsilon}$	$\overline{\zeta}$	$\overline{\varepsilon}$	$\overline{\zeta}$	$\overline{\varepsilon}$
0.0	$2.371923675753622{\cdot}10^{-2}$	1.0	$4.4290728085271487{\cdot}10^{-4}$	2.0	$1.473550679584063{\cdot}10^{-4}$	3.0	$2.7649200449062134{\cdot}10^{-4}$
0.1	$5.686808624153531{\cdot}10^{-4}$	1.1	$6.652891785879232{\cdot}10^{-4}$	2.1	$5.687985324178502{\cdot}10^{-5}$	3.1	$4.247287635803276{\cdot}10^{-4}$
0.2	$1.3997667927872804{\cdot}10^{-4}$	1.2	$9.384050608695733{\cdot}10^{-4}$	2.2	$1.0798603815693152{\cdot}10^{-4}$		
0.3	$9.102151236315801{\cdot}10^{-5}$	1.3	$1.3634955866821423{\cdot}10^{-3}$	2.3	$1.0594306174653013{\cdot}10^{-4}$		
0.4	$1.8717833198870506{\cdot}10^{-4}$	1.4	$1.3448550578190593{\cdot}10^{-3}$	2.4	$8.571922589199749{\cdot}10^{-5}$		
0.5	$4.2526882623132416{\cdot}10^{-4}$	1.5	$1.2132174532651582{\cdot}10^{-3}$	2.5	$7.289038598104997{\cdot}10^{-5}$		
0.6	$5.702431727029635{\cdot}10^{-4}$	1.6	$1.5748365953251152{\cdot}10^{-3}$	2.6	$7.472151940658472{\cdot}10^{-5}$		
0.7	$6.072199441558427{\cdot}10^{-4}$	1.7	$1.1624567352066994{\cdot}10^{-3}$	2.7	$1.0595592222444953{\cdot}10^{-4}$		
0.8	$3.0232443172091886{\cdot}10^{-4}$	1.8	$9.761812513876445{\cdot}10^{-4}$	2.8	$1.8547222673526522{\cdot}10^{-4}$		
0.9	$5.887059560416711{\cdot}10^{-4}$	1.9	$4.747211161658764{\cdot}10^{-4}$	2.9	$1.7730523519636827{\cdot}10^{-4}$		

The right-hand side of Eq. (46) shows that this term is diffusive, tending to redistribute the TKE throughout the PBL. As the TKE, e, is not available from observations, it is approximated here by a parameterization in terms of the time-averaged TKE dissipation rate, $\overline{\varepsilon}$, employing the following relation (Stull 1997, Eq. (6.5f) therein):

$$K_M = c_\varepsilon \frac{e^2}{\overline{\varepsilon}} \quad \rightsquigarrow \quad e = \sqrt{\frac{K_M \overline{\varepsilon}}{c_\varepsilon}} \,, \quad c_\varepsilon = 0.09 \,. \tag{47}$$

Figure 22 shows the TKE, $e = \sqrt{K_M \overline{\varepsilon}/c_\varepsilon}$, determined according to Eq. (47). According to the assumed constancy of the eddy diffusivity the maxima in the $e(z)$ profile follow those in the $\overline{\varepsilon}(z)$ profile.

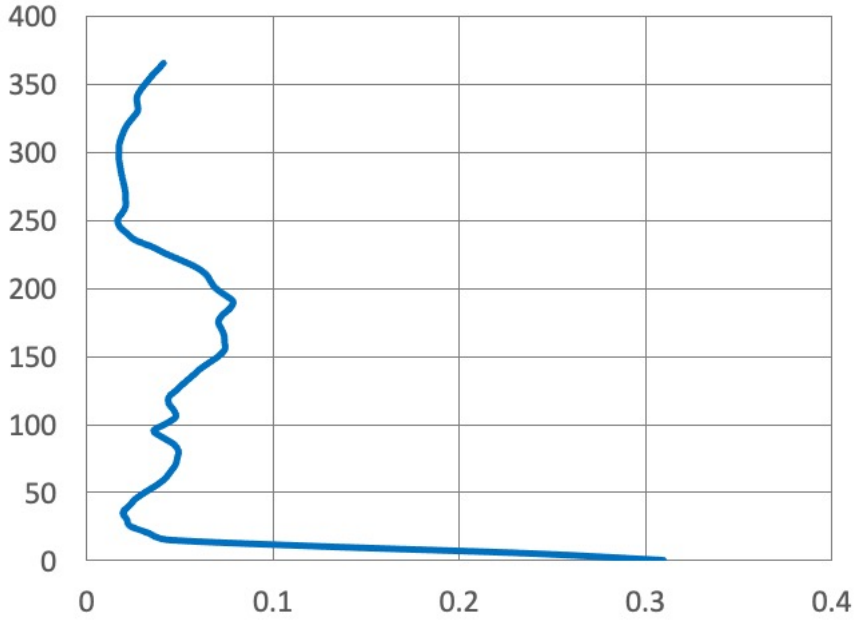

Figure 22: Vertical profile of the TKE, $e = \sqrt{K_M \overline{\varepsilon}/c_\varepsilon}$, determined according to Eq. (47). The abscissa shows e in units of $\mathrm{m}^2\,\mathrm{s}^{-2}$, the ordinate the height level z in units of m.

Inserting Eq. (47) into Eq. (46) the TKE redistribution term reads:

$$\left(\frac{\partial e}{\partial t}\right)_T \approx K_M \frac{\partial^2 e}{\partial z^2} = \frac{1}{2}\sqrt{\frac{K_M^3}{c_\varepsilon \overline{\varepsilon}}} \left[\frac{\partial^2 \overline{\varepsilon}}{\partial z^2} - \frac{1}{2\overline{\varepsilon}}\left(\frac{\partial \overline{\varepsilon}}{\partial z}\right)^2\right] \,. \tag{48}$$

In **Fig. 23** the vertical profile of the TKE redistribution term $(\partial e/\partial t)_T$ according to Eqs. (33) and (48), respectively, is shown. The $(\partial e/\partial t)_T$ profile exhibits two distinct peaks: one maximum TKE loss rate at $z \approx 20\,\mathrm{m}$, and one maximum TKE production closely above at $z \approx 25 - 30\,\mathrm{m}$. These opposite peaks tend to remove the strong TKE gradient appearing close to the surface at $z < 50\,\mathrm{m}$. Similarly, the rapidly alternating TKE rates around the inversion height also tend to "eqilibrate" the TKE profile.

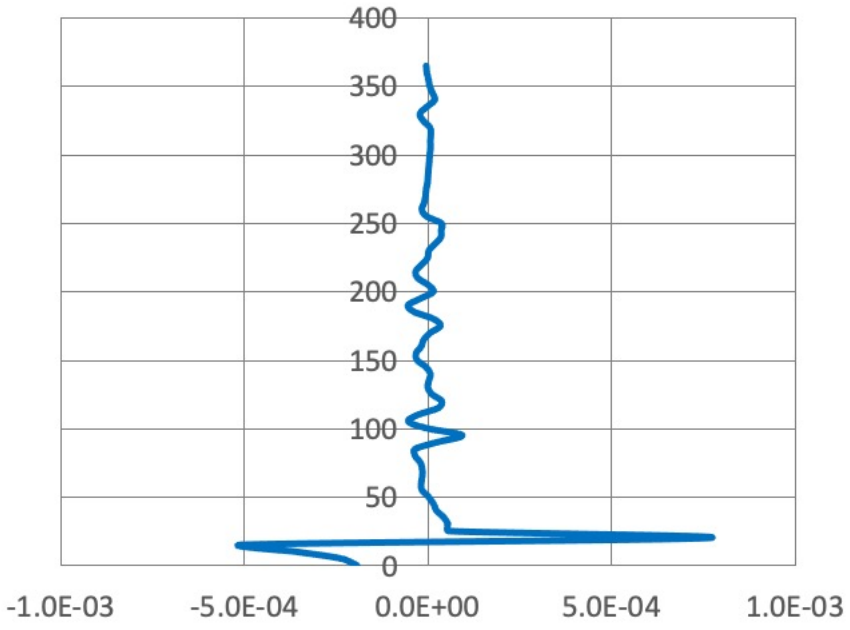

Figure 23: Vertical profile of the parameterized TKE redistribution, $(\partial e/\partial t)_T$ according to Eqs. (33) and (48, respectively. The abscissa shows $(\partial e/\partial t)_T$ in units of $\mathrm{m}^2\,\mathrm{s}^{-3}$, the ordinate the height level z in units of m.

4.6 Comparison of the single contributions to the total time rate of TKE change

Figures 24 and **25** display the time rates of change contributing to the TKE budget including the shear-induced production $(\partial e/\partial t)_S$ (graph 1, black dashed), the buoyancy-induced loss $(\partial e/\partial t)_B$ (graph 2, red), the dissipation-induced loss $(\partial e/\partial t)_D$ (graph 3, green), the redistribution $(\partial e/\partial t)_T$ (graph 4, light-blue), and the total time rate of TKE change $(\partial e/\partial t)$ (graph 5, black solid). In **Fig. 24** the shear-induced contribution $(\partial e/\partial t)_S$ is determined using the simulated $v(z)$ profile, and in **Fig. 25** using the observed $v(z)$ profile. Both approaches lead to remarkable differences in the total time rate of TKE change (graph 5, black solid). A common feature in both cases is the pronounced TKE loss close to the surface due to TKE dissipation into heat. However, while the employment of the simulated $v(z)$ profile in the determination of $(\partial e/\partial t)_S$ results in a remarkable shear-induced TKE production close to the surface, the use of the observed $v(z)$ profile leads to remarkable shear-induced TKE production at the LLJ level. The use of the simulated wind profile results in an overall TKE loss throughout the ABL, while the use of the observed wind profile leads to a net TKE production at the LLJ level.

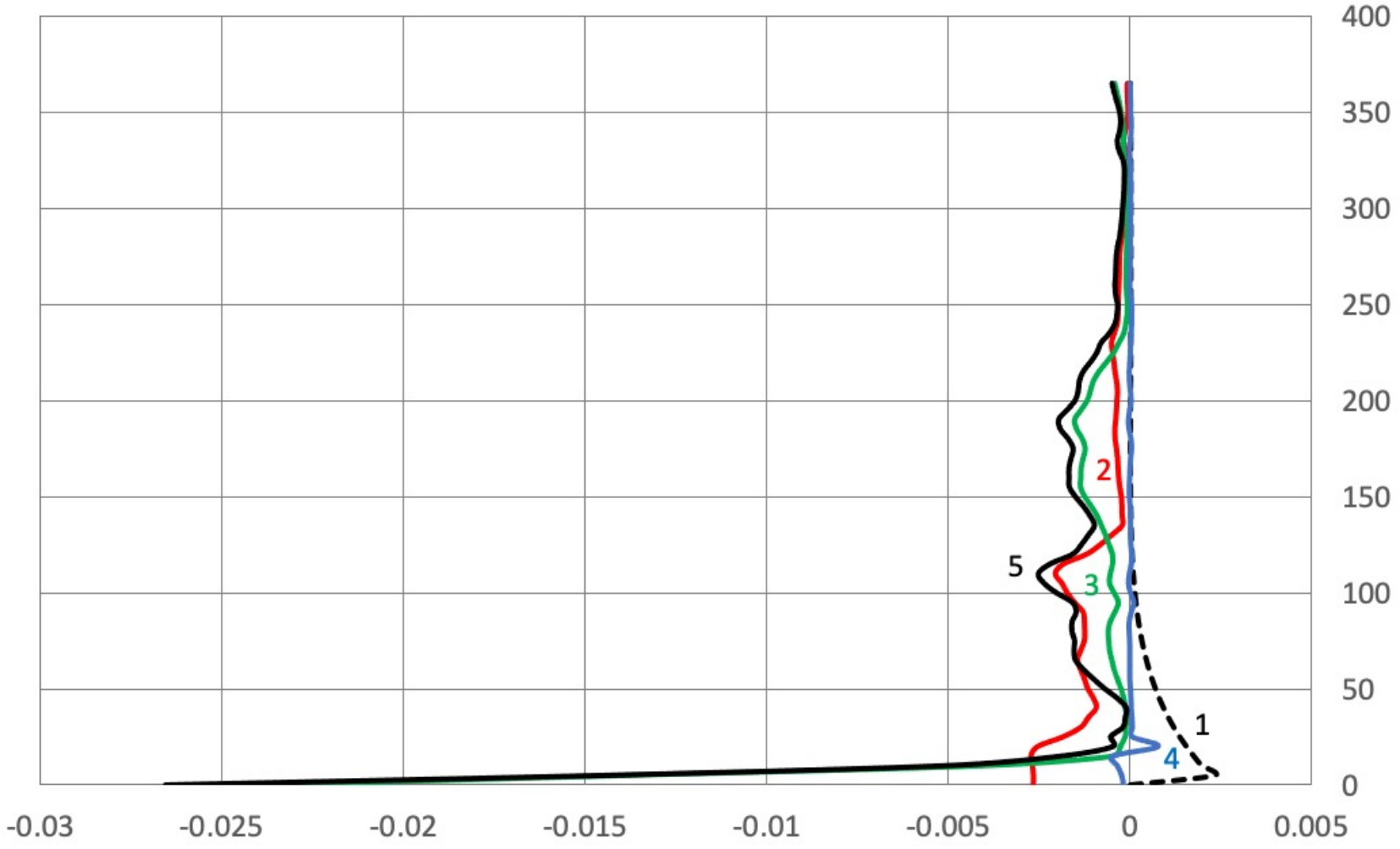

Figure 24: Vertical profiles of the contributions to the TKE budgets: shear-induced contribution $(\partial e/\partial t)_S$ employing the **simulated** $v(z)$ profile (graph 1, black dashed), buoyancy-induced contribution $(\partial e/\partial t)_B$ (graph 2, red), dissipation-induced contribution $(\partial e/\partial t)_D$ (graph 3, green), redistribution contribution $(\partial e/\partial t)_T$ (graph 4, light-blue), total time rate of TKE change $(\partial e/\partial t)$ (graph 5, black solid), The abscissa shows the $(\partial e/\partial t)$ terms in units of $\mathrm{m}^2\,\mathrm{s}^{-3}$, the ordinate the height level z in units of m.

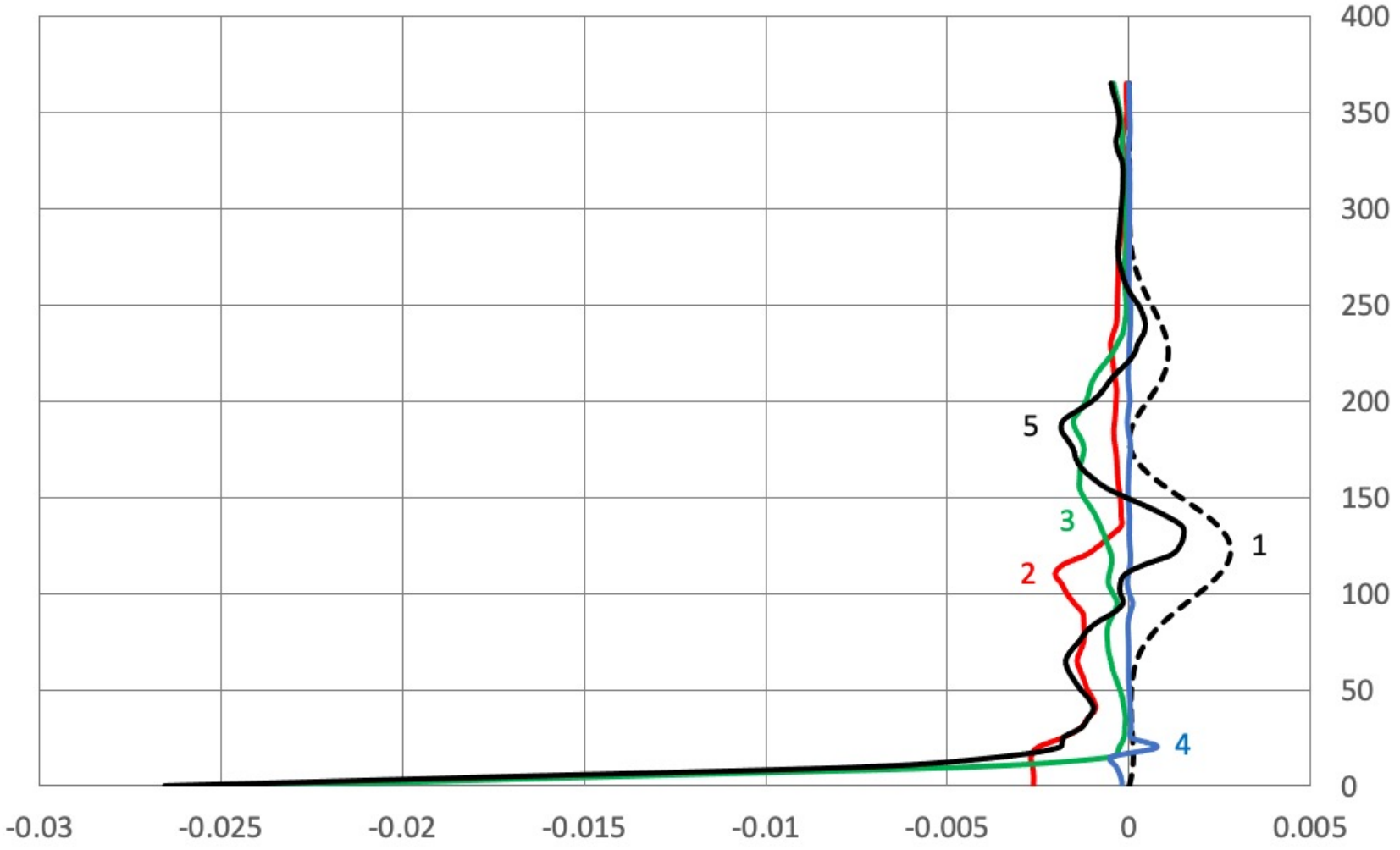

Figure 25: Vertical profiles of the contributions to the TKE budgets: shear-induced contribution $(\partial e/\partial t)_S$ employing the **observed** $v(z)$ profile (graph 1, black dashed), buoyancy-induced contribution $(\partial e/\partial t)_B$ (graph 2, red), dissipation-induced contribution $(\partial e/\partial t)_D$ (graph 3, green), redistribution contribution $(\partial e/\partial t)_T$ (graph 4, light-blue), total time rate of TKE change $(\partial e/\partial t)$ (graph 5, black solid), The abscissa shows the $(\partial e/\partial t)$ terms in units of $\mathrm{m}^2\,\mathrm{s}^{-3}$, the ordinate the height level z in units of m.

5 LLJ implications for the transport of a passive tracer

5.1 Model description: advection-diffusion equation

To assess the impact of the LLJ on the transport of a passive tracer here a special solution of the advection-diffusion equation (ADE, Eq. (49)), will be discussed:

$$\begin{aligned}\frac{\partial c(x,y,z,t)}{\partial t} &= \frac{\partial}{\partial x}\left[D_x(x,y,z,t)\frac{\partial c(x,y,z,t)}{\partial x} - v_x(x,y,z,t)c(x,y,z,t)\right] \\ &+\frac{\partial}{\partial y}\left[D_y(x,y,z,t)\frac{\partial c(x,y,z,t)}{\partial y} - v_y(x,y,z,t)c(x,y,z,t)\right] \\ &+\frac{\partial}{\partial z}\left[D_z(x,y,z,t)\frac{\partial c(x,y,z,t)}{\partial z} - v_z(x,y,z,t)c(x,y,z,t)\right] \\ &-\mu c(x,y,z,t) + q(x,y,z,t)\ .\end{aligned} \tag{49}$$

In Eq. (49), $c(x,y,z,t)$ denotes the concentration the passive tracer in arbitrary units (a.u.), v_x, v_y, and v_z are the components of the wind vector, the quantities D_x, D_y, and D_z are the diffusion coefficients for the turbulent exchange of the passive tracer in x-, y-, and z-directions, μ is the decay constant, and the non-homogeneous term $q(x,y,z,t)$ represents the source of the pollutent mass or number injected at the position (x,y,z) and time t. The initial condition reads:

$$c(x,y,z,t=0) = 0\ . \tag{50}$$

The advection-diffusion equation is simplified as follows:

- According to Eqs. (10) and (11), the horizontal wind field is assumed to be horizontally homogeneous, i.e., the horizontal wind components depend only on height and time, $v_x(x,y,z,t) = v_x(z,t)$ and $v_y(x,y,z,t) = v_y(z,t)$.

- The air flow with mass density ϱ is assumed to be incompressible, i.e.,

$$\frac{1}{\varrho}\frac{\mathrm{d}\varrho}{\mathrm{d}t} = -\left(\frac{\partial v_x}{\partial x} + \frac{\partial v_y}{\partial y} + \frac{\partial v_z}{\partial z}\right) = 0\ .$$

- As a consequence of the horizontal homogeneity of the air flow,

$$\frac{\partial v_x}{\partial x} = \frac{\partial v_y}{\partial y} = 0\ ,$$

  one has:

$$\frac{\partial v_z}{\partial z} = 0 \quad \rightsquigarrow \quad v_z(z,t) = \text{const.} \tag{51}$$

  At the lower boundary impermeability of the surface is assumed, i.e., $v_z(z=0,t) = 0$. By virtue of Eq. (51) the vertical wind velocity must vanish throughout the ABL, i.e., $v_z(z,t) = 0$.

- As the x-axis is aligned parallel to the isobars (i.e., in the direction of the geostrophic wind according to Eq. (15)), the horizontal wind velocity, $|\vec{v}|$, is dominated by the x-component of the horizontal wind, v_x. For this reason, horizontal tracer advection normal to the isobars is neglected.

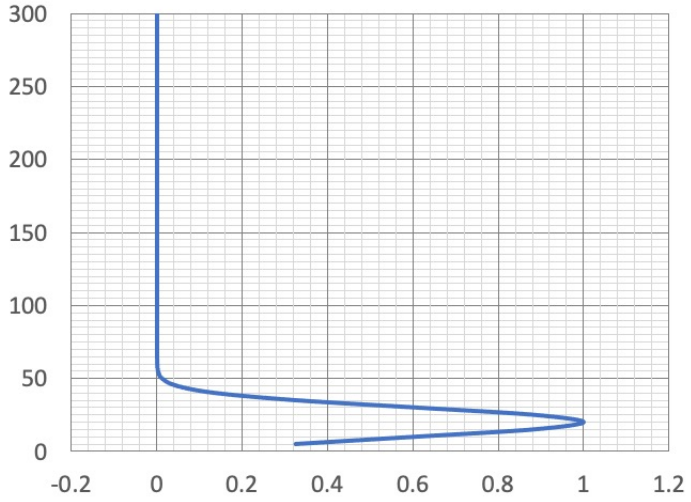

Figure 26: Vertical profile of the tracer source according to Eq. (52) with $q_0 = 1.0\,\mathrm{a.u.\,s^{-1}}$, $z_0 = 20\,\mathrm{m}$, and $\sigma_z = 10\,\mathrm{m}$. The abscissa shows q_0 in units of $\mathrm{a.u.\,s^{-1}}$ and the ordinate the height z in units of m.

- Turbulent diffusion in x- and y-directions is neglected, i.e., $D_x = D_y \approx 0$. The turbulent diffusion in vertical direction is optionally allowed to depend on height, i.e., $D_z(x, y, z, t) = D_z(z)$. The eddy diffusivity for the turbulent tracer transport is approximated by that for the turbulent heat transport, i.e., $D_z(z) \approx K_H(z)$. Corresponding to the assumptions underlying the Shapiro-Fedorovich model, $K_H = \mathrm{const.}$ is assumed.

- The tracer is assumed to be passive without decay, i.e., $\mu = 0$.

- The tracer is assumed to be continously emitted in time according to the following source specification (see **Fig. 26**):

$$q(x, z, t) = q_0(x_0, t) \exp\left[-\frac{1}{2}\left(\frac{z - z_0}{\sigma_z}\right)^2\right] . \tag{52}$$

  Here, $x = x_0$ and $z = z_0$ specify the location of the tracer injection, and σ_z is the measure of the dispersion width of the tracer injection. The quantity q_0 is the source strength in units of $\mathrm{a.u.}/\mathrm{s}$. In the present case a near-surface emission source at $z_0 = 20\,\mathrm{m}$ with $\sigma_z = 10\,\mathrm{m}$, and $q_0 = 1\,\mathrm{a.u.\,s^{-1}}$ is assumed.

- The tracer flux at the surface is assumed to be equal to the particle deposition flux $(\overline{v_z' c'})_s = -v_d c(z_1)$ with v_d denoting the deposition velocity and $c(z_1)$ the tracer concentration at height of the first main level z_1. For the deposition velocity $v_d = 0.01\,\mathrm{m\,s^{-1}}$ is assumed, which corresponds to a particle diameter of $D_p = 0.5\,\mu\mathrm{m}$ (Bleyl 2001,p. 62). The tracer flux at the top of the model is assumed to vanish, $(\overline{v_z' c'})_t = 0$, i.e., neither entrainment nor detrainment of air shall occur.

With these assumptions the ADE reduces to the following two-dimensional form:

$$\begin{aligned} \frac{\partial c(x,z,t)}{\partial t} &\approx -v_x(z,t)\frac{\partial c(x,z,t)}{\partial x} + K_H \frac{\partial^2 c(x,z,t)}{\partial z^2} + q(x,z,t) \ , \\ & 0 \le x \le x_{max} \ , \quad 0 \le z \le z_{max} \ . \end{aligned} \tag{53}$$

In x-direction the model domain has an extension of $X_{\max} = 80\,\mathrm{km}$, which is discretized in $j_{\max} = 160$ grid points according to $x_j = (j-1)\Delta x$, $j = 1, \ldots, j_{\max}$ with $\Delta x = 500\,\mathrm{m}$. In y-direction the model domain has an extension of $Z_{\max} = 300\,\mathrm{m}$, which is discretized in $k_{\max} = 60$ grid points according to $z_k = (k-1)\Delta z$, $k = 1, \ldots, k_{\max}$ with $\Delta z = 5\,\mathrm{m}$.

5.2 Case studies

5.2.1 Pre-LLJ conditions

The pre-LLJ conditions serve as the reference case. The wind profile is given by the x-component of the stationary Ekman helix, Eq. (18),

$$v_x(z) = u_g \left[1 - \exp(-\gamma_E z)\cos(\gamma_E z)\right] \ , \quad \gamma_E = \sqrt{\frac{f}{2K_{M,0}}} \ . \tag{54}$$

The pre-LLJ eddy diffusivity of momentum amounts $K_{M,0} = 3.7\,\mathrm{m^2\,s^{-1}}$ (according to **Table 5**). Assuming $\mathrm{Pr}_t = 0.7$, the corresponding pre-LLJ eddy diffusivity of heat amounts $K_{H,0} = K_{M,0}/\mathrm{Pr}_t \approx 5.3\,\mathrm{m^2\,s^{-1}}$ according to Eq. (30).

5.2.2 LLJ conditions

The LLJ conditions serce as the comparative case. The wind profile is given by the x-component of the instationary horizontal wind field according to the Shapiro-Fedorovich solution, Eq. (20),

$$v_x(z,t) = u_g V_x(Z, T_t) \ , \quad Z = z\sqrt{\frac{f}{K_{M,0}}} \ , \quad T_t \equiv ft \ , \tag{55}$$

with $V_x(Z, T_t)$ given by Eq. (21). The LLJ-phase eddy diffusivity of momentum amounts $K_M = kK_M, 0 \approx 0.36\,\mathrm{m^2\,s^{-1}}$ (according to **Table 5**) Assuming $\mathrm{Pr}_t = 0.7$, the corresponding LLJ eddy diffusivity of heat amounts $K_{H,0} = K_{M,0}/\mathrm{Pr}_t \approx 0.514\,\mathrm{m^2\,s^{-1}}$ according to Eq. (30).

5.3 Results

Figures 27 and **28** show the spatial distribution of the tracer concentration $c(x, z, t)$ under pre-LLJ (top panel) and LLJ conditions (bottom panel) at dimensionless times $T = 0.5$ (**Fig. 27**) and $T = 3$ (**Fig. 28**.) The higher eddy diffusivity during pre-LLJ conditions leads to a much stronger diluation of the released passive tracer than under LLJ conditions in the early stage of the time evolution (**Fig. 27**).

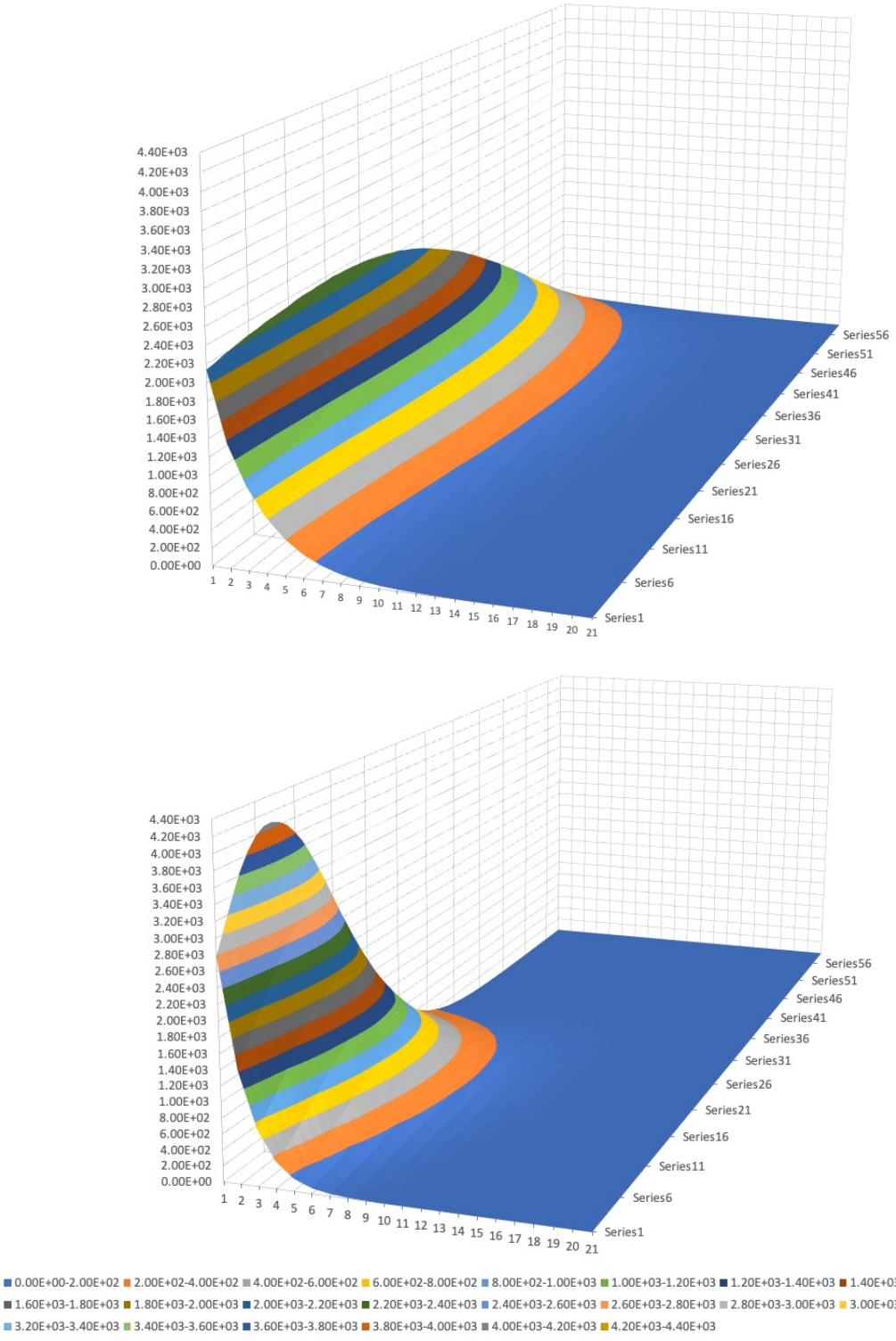

Figure 27: Tracer concentration $c(x, z, t)$ in arbitrary units (a.u.) as function of horizontal grid-point index j (lower abscissa) and vertical grid-point index k (right-hand side abscissa, series 1-60) at dimensionless time $T = 0.5$. Top panel: pre-LLJ phase; bottom panel: LLJ phase.

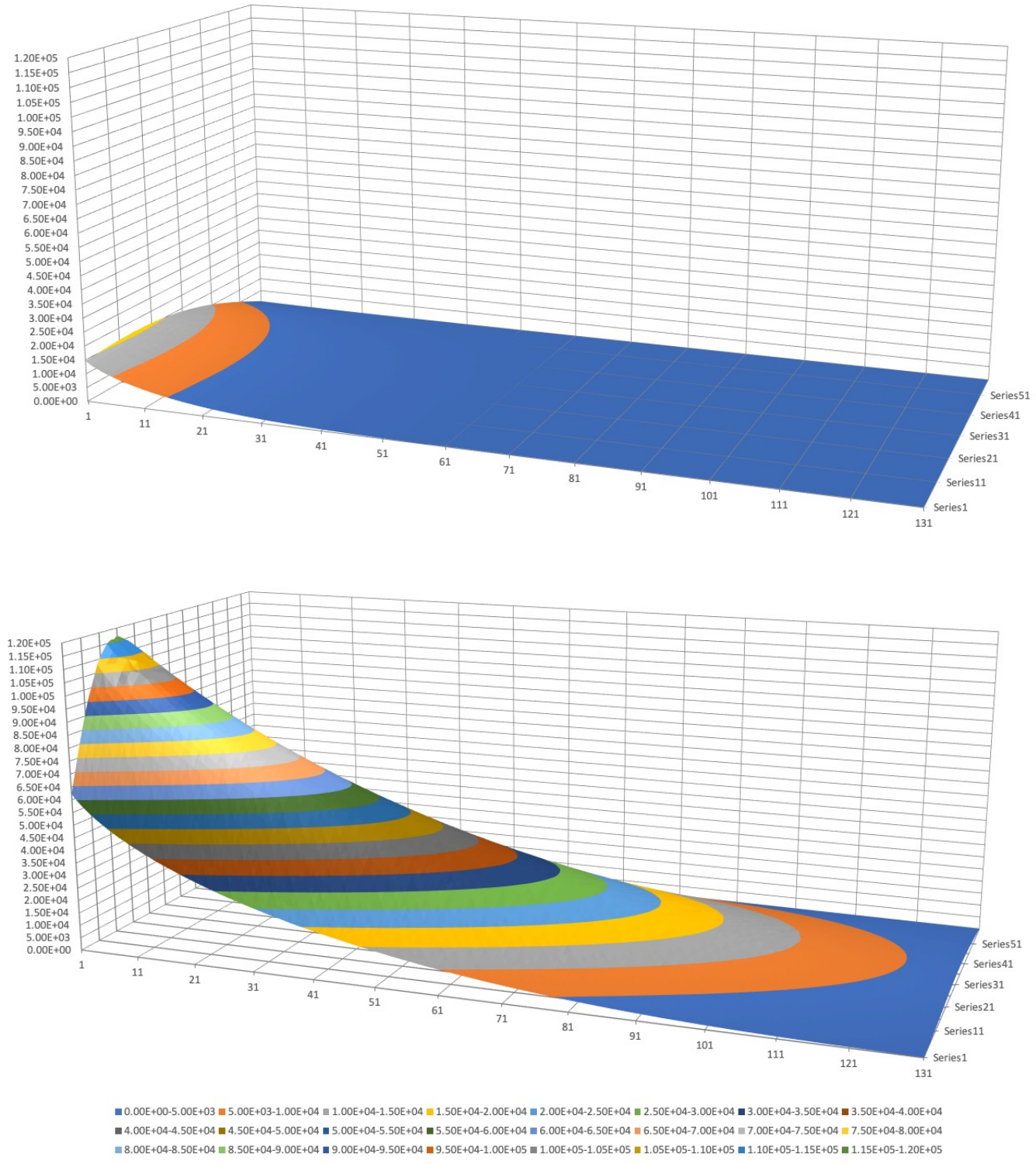

Figure 28: As Fig. 27 but at dimensionless time $T = 3.0$.

The tracer distribution at $T = 3.0$ (**Fig. 28**) shows that the smaller diffusion and higher advective transport under LLJ conditions leads to an enhancement of the tracer concentration in remote regions. A similar diffuse and advective transport effect is expectable for reactive tracers involved in the formation of precursor gases. As a consequence, LLJs can have a siginificant impact on in situ and ex situ aerosol formation and evolution under Arctic conditions.

Acknowledgement

The authors acknowledge the essential help of Andreas Herber, Jens Voigtländer, Frank Stratmann, and the crew of Station Nord and Villum Research Station during the balloon operations. Special thanks go to Sven-Erik Gryning for data provisioning and advisory service on ceilometer and wind lidar data at VRS, and to Andreas Massling, Daniel Charles Thomas, and Jakob Boyd Pernov for discussing VRS data. The Deutsche Forschungsgemeinschaft (DFG, German Research Foundation) is gratefully acknowledged for the project funding (project number 268020496 - TRR 172) within the Transregional Collaborative Research Center "ArctiC Amplification: Climate Relevant Atmospheric and SurfaCe Processes, and Feedback Mechanisms (AC)^3" in sub-project A02. The data is publicly available (Egerer et al. 2019). The contribution of Olaf Hellmuth was provided within the TROPOS research topic "Atmospheric aerosols: Process studies on small spatial and temporal scales".

A The concept of "effective" eddy diffusivity

A.1 Interpretation of the effective eddy diffusivity as the vertical arithmetic mean value

The application of the similarity function concept within the framework of local similarity allows the parameterization of turbulent fluxes for the whole SBL (Heinemann 2004). The eddy diffusivities K_A for momentum (A=M) and heat (A=H) can be expressed in terms of the Monin-Obukhov length L as follows (Heinemann 2004, Eq. (3a) therein):

$$K_A = \frac{\kappa u_\star z}{\varphi_A(\zeta)} \;, \quad \zeta = \frac{z}{L} \;. \tag{A.1}$$

In Eq. (A.1), κ denotes the von Karman constant, and φ_A is the similarity function. For stable conditions φ_A is often described as a linear function of the dimensionless height ζ (Heinemann 2004, Eq. (3b) therein):

$$\varphi_A = 1 + A_A\zeta \;, \quad A_M = 6 \;. \tag{A.2}$$

Now, one can define an "effective" eddy diffusivity as the vertical mean of $K_A(z)$ over the SBL height h:

$$\overline{K}_A \equiv \frac{1}{h}\int_0^h K_A(z)\,\mathrm{d}z = \frac{\kappa u_\star}{ha^2}\left[ah - \ln(ah+1)\right] \;, \quad a = \frac{A_A}{L} \;. \tag{A.3}$$

Analogously, one can define a corresponding "effective" height z_{eff}, at which the local eddy diffusivity K_A equals the arithmetic mean eddy diffusivity $\overline{K}_A$:

$$K_A(z_{\text{eff}}) = \overline{K}_A \quad \rightsquigarrow \quad \frac{z_{\text{eff}}}{h} = \frac{ah - \ln(1+ah)}{ah\ln(1+ah)} \;. \tag{A.4}$$

By virtue of $\partial K_A/\partial z = K_A/(\varphi_A z) > 0$ the eddy diffusivity increases with height. Analogously, by virtue of $\partial K_A/\partial L = K_A A_A z/(\varphi_A L^2) > 0$, the eddy diffusivity increases with increasing L (see **Table A.1**). **Table A.2** shows the normalized effective height z_{eff}/h as function of L according to Eq. (A.4) for $h = \overline{z}_{inv} = 118\,\mathrm{m}$.

A.2 Interpretation of the effective eddy diffusivity as the vertical harmonic mean value

Interpreting the LLJ-phase eddy diffusivity as the vertical harmonic mean results in

$$\frac{1}{\widetilde{K}_A} = \frac{1}{h-z_0}\int_{z_0}^h \frac{\mathrm{d}z}{K_A(z)} = \frac{1}{\kappa u_\star(h-z_0)}\left[\ln\frac{h}{z_0} + \frac{A}{L}(h-z_0)\right] \;. \tag{A.5}$$

In this case one can define a corresponding "effective" height z_{eff}, at which the local eddy diffusivity K_A equals the harmonic mean eddy diffusivity $\overline{K}_A$:

$$K_A(z_{\text{eff}}) = \widetilde{K}_A \quad \rightsquigarrow \quad \frac{z_{\text{eff}}}{h} = \frac{h-z_0}{h\ln\dfrac{h}{z_0}} \approx \frac{1}{\ln\dfrac{h}{z_0}} \;. \tag{A.6}$$

Table A.1: Normalized eddy diffusivity $K_M/(\kappa u_\star h)$ according to Eqs. (A.1) and (A.2) for $A_M = 6$ as function of the normalized height z/h for different values of the Monin-Obukhov length L.

z/h	L/m			
	1	10	100	1000
0.00	0.00	0.00	0.00	0.00
0.08	0.01	0.05	0.08	0.08
0.17	0.02	0.11	0.16	0.17
0.25	0.04	0.16	0.24	0.25
0.34	0.05	0.21	0.32	0.34
0.42	0.06	0.26	0.40	0.42
0.51	0.07	0.32	0.48	0.51
0.59	0.08	0.37	0.56	0.59
0.68	0.10	0.42	0.64	0.67
0.76	0.11	0.48	0.72	0.76
0.85	0.12	0.53	0.80	0.84
0.93	0.13	0.58	0.88	0.93
1.02	0.15	0.64	0.96	1.01

Table A.2: Normalized "effective" height, z_{eff}/h, at which the local eddy diffusivity K_A equals the mean eddy diffusivity, $\overline{K}_M$, calculated for different values of the Monin-Obukhov length.

L/m	1	5	10	25	50	100	1000
z_{eff}/h	0.15	0.19	0.22	0.26	0.3	0.34	0.46

Assuming $z_0 \approx 10^{-2}\,\mathrm{m}$ and $h = 10^2\,\mathrm{m}$, one obtains $z_{\mathrm{eff}}/h \approx 0.11$ according to Eq. (A.6). In searching for the value of the turbulent eddy diffusivity of momentum, K_M, which is characteristic for the whole PBL, Malcher and Kraus (1983) employed in their LLJ modelling study the ad hoc ansatz $K_M = \kappa u_\star z_a$ and obtained good results with $z_a = 1.25\,\mathrm{m}$ for stable stratification, and otherwise $z_a = 10\,\mathrm{m}$. On the other side, ReVelle and Nilsson (2008) proposed the form $K_M = \kappa u_\star z_{inv}$ with z_{inv} denoting the LLJ altitude (assumed to be the top of the nocturnal inversion layer at sunset and constant throughout the night). The characteristic length scale estimated here employing the concept of the effective eddy diffusivity is constrained by the inequality $z_a \leq z_{\mathrm{eff}} \leq h$.

B Approximations employed in the time averaging

Introducing the annotations $y = (u_{h,obs}, z)$ and $y_0 = (u_{h,max,obs}, z_i)$, approximating the time averaging by the arithmetic mean of a sample $\{y_i, y_{0,i}\}$, $i = 1, \ldots, N$, and representing the actual values of the observable y_i and the scaling quantity $y_{0,i}$ by the superposition

of their mean values $\overline{y}$, $\overline{y}_0$ and the corresponding actual deviations δy_i, $\delta y_{0,i}$,

$$\begin{aligned} y_i &= \overline{y} + \delta y_i \ , \quad y_{0,i} = \overline{y}_0 + \delta y_{0,i} \ , \\ \overline{y} &= \frac{1}{N}\sum_{i=1}^{N} y_i \ , \quad \overline{y}_0 = \frac{1}{N}\sum_{i=1}^{N} y_{0,i} \ , \\ \overline{\delta y} &= \frac{1}{N}\sum_{i=1}^{N} \delta y_i = 0 \ , \quad \overline{\delta y_0} = \frac{1}{N}\sum_{i=1}^{N} \delta y_{0,i} = 0 \ , \end{aligned}$$

one arrives at the following relation for the averaged normalized quantity $\overline{y}_n$:

$$\begin{aligned} \overline{y}_n &= \frac{1}{N}\sum_{i=1}^{N}\left(\frac{y_i}{y_{0,i}}\right) = \frac{1}{N}\sum_{i=1}^{N}\left(\frac{y_i}{\overline{y}_0 + \delta y_{0,i}}\right) = \frac{1}{N}\sum_{i=1}^{N}\left(\frac{y_i}{\overline{y}_0\left(1 + \dfrac{\delta y_{0,i}}{\overline{y}_0}\right)}\right) \\ &\approx \frac{1}{N}\sum_{i=1}^{N}\left(\frac{y_i}{\overline{y}_0}\right)\left(1 - \frac{\delta y_{0,i}}{\overline{y}_0}\right) = \frac{\overline{y}}{\overline{y}_0} - \frac{1}{N}\sum_{i=1}^{N}\left(\frac{y_i\,\delta y_{0,i}}{\overline{y}_0^2}\right) \\ &= \frac{\overline{y}}{\overline{y}_0}\left[1 - \frac{1}{N}\sum_{i=1}^{N}\left(\frac{\delta y_i\,\delta y_{0,i}}{\overline{y}\,\overline{y}_0}\right)\right] \ . \end{aligned} \tag{B.1}$$

If the assumption

$$\frac{\overline{\delta y\,\delta y_0}}{\overline{y}\,\overline{y}_0} \ll 1 \ , \quad \overline{\delta y\,\delta y_0} = \frac{1}{N}\sum_{i=1}^{N}\delta y_i\,\delta y_{0,i}$$

is valid, one arrives at the approximation $\overline{y}_n \approx \overline{y}/\overline{y}_0$, from which the dimensioned mean quantity $\overline{y}$ can be calculated by $\overline{y} \approx \overline{y}_n\overline{y}_0$.

References

Beyrich, F. and Klose, B.: Modellierung nächtlicher niedertroposphärischer Windmaxima. I.Theoretische Betrachtungen, Z. Meteorol., 6, 333–347, 1987.

Beyrich, F. and Klose, B.: Modellierung nächtlicher niedertroposphärischer Windmaxima. II.Modellverifikation, Z. Meteorol., 40, 30–37, 1990.

Blackadar, A. K.: Boundary layer wind maxima and their significance for the growth of nocturnal inversions, Bulletin of the American Meteorological Society, 38, 283–290, doi:10.1175/1520-0477-38.5.283, `https://journals.ametsoc.org/view/journals/bams/38/5/1520-0477-38_5_283.xml`, 1957.

Bleyl, M. R.: Experimentelle Bestimmung der Depositionsgeschwindigkeit luftgetragener Partikel mit Hilfe der Eddy-Kovarianzmethode über einem Fichtenbestand im Solling, Ph.D. thesis, Georg-August-Universität zu Göttingen, Mathematisch-Naturwissenschaftliche Fakultät, 149 pp., 2001.

Egerer, U., Siebert, H., Voigtländer, J., and Gottschalk, M.: Tethered balloon-borne measurements of turbulence and radiation during the Arctic field campaign PAMARCMiP in March/ April 2018, doi:10.1594/PANGAEA.900240, 2019.

Egerer, U., Siebert, H., Hellmuth, O., and Sørensen, L. L.: The role of a low-level jet for stirring the stable atmospheric surface layer in the Arctic, to be subm. to Atmos. Chem. Phys., 2023.

Fiedler, S., Schepanski, K., Heinold, B., Knippertz, P., and Tegen, I.: Climatology of nocturnal low-level jets over North Africa and implications for modeling mineral dust emission, Journal of Geophysical Research: Atmospheres, 118, 6100–6121, doi:https://doi.org/10.1002/jgrd.50394, https://agupubs.onlinelibrary.wiley.com/doi/abs/10.1002/jgrd.50394, 2013.

Grachev, A., Andreas, E., Fairall, C., Guest, P., and Persson, P. G.: On the turbulent Prandtl number in the stable atmospheric boundary layer, Boundary-Layer Meteorology, pp. 329–341, 2007.

Heinemann, G.: Local similarity properties of the continuously turbulent stable boundary layer over Greenland, Boundary-Layer Meteorology, 112, 283–305, 2004.

Heinemann, G., Drüe, C., Schwarz, P., and Makshtas, A.: Observations of wintertime low-level jets in the coastal region of the Laptev Sea in the Siberian Arctic using SODAR/RASS, Remote Sensing, 13, doi:10.3390/rs13081421, https://www.mdpi.com/2072-4292/13/8/1421, 2021.

Hendriksen (ed.), N. B.: Villum Research Station, Station Nord. 2018 Annual Report, Tech. rep., Villum Research Station, Station Nord, Aarhus University, https://villumresearchstation.dk/annual-reports/, 2019.

Holtslag, A. A. M.: Surface fluxes and boundary layer scaling. Models and applications, Scientific Report WR 87-2(FM), Koninklijk Nederlands Meteorologisch Instituut, De Bilt, 1987.

Kottmeier, C., Lege, D., and Roth, R.: Ein Beitrag zur Klimatologie und Synoptik der Grenzschichtstrahlströme über der Norddeutschen Tiefebene, Ann. Meteorol. (NF), 20, 18–19, 1983.

Lenschow, D. H., Li, X. S., Zhu, C. J., and Stankov, B. B.: The stably stratified boundary layer over the Great Plains. I. Mean and turbulence structure, Boundary-Layer Meteorology, 42, 95–121, 1988.

Li, D.: Turbulent Prandtl number in the atmospheric boundary layer - where are we now?, Atmospheric Research, 216, 86–105, doi:https://doi.org/10.1016/j.atmosres.2018.09.015, https://www.sciencedirect.com/science/article/pii/S0169809518307324, 2019.

López-García, V., Neely, Ryan R., I., Dahlke, S., and Brooks, I. M.: Low-level jets over the Arctic Ocean during MOSAiC, Elementa: Science of the Anthropocene, 10, doi:10.1525/elementa.2022.00063, https://doi.org/10.1525/elementa.2022.00063, 2022.

Malcher, J. and Kraus, H.: Low-level jet phenomena described by an integrated dynamical PBL model, Boundary-Layer Meteorol., 27, 327–343, https://doi.org/10.1007/BF02033743, 1983.

Mix, W.: Empirische Befunde über die vertikale Verteilung des horizontalen Windvektors an niedertroposphärischen Inversionen unter besonderer Beachtung des Low-Level-Jet, Z. Meteorol., 31, 220–242, 1981.

Nieuwstadt, F. T. M.: The turbulent structure of the stable, nocturnal boundary layer, Journal of Atmospheric Sciences, 41, 2202–2216, doi:10.1175/1520-0469(1984)041<2202:TTSOTS>2.0.CO;2, https://journals.ametsoc.org/view/journals/atsc/41/14/1520-0469_1984_041_2202_ttsots_2_0_co_2.xml, 1984.

Press, W. H., Teukolsky, S. A., Vetterling, W. T., and Flannery, B. P.: Numerical Recipes in Fortran 77. The Art of Scientific Computing. Second Edition. Volume 1 of Fortran Numerical Recipes, Cambridge University Press, New York, 1996.

ReVelle, D. O. and Nilsson, E. D.: Summertime Low-Level Jets over the High-Latitude Arctic Ocean, Journal of Applied Meteorology and Climatology, 47, 1770 – 1784, doi:10.1175/2007JAMC1637.1, https://journals.ametsoc.org/view/journals/apme/47/6/2007jamc1637.1.xml, 2008.

Shapiro, A. and Fedorovich, E.: Analytical description of a nocturnal low-level jet, Quarterly Journal of the Royal Meteorological Society, 136, 1255–1262, doi:https://doi.org/10.1002/qj.628, https://rmets.onlinelibrary.wiley.com/doi/abs/10.1002/qj.628, 2010.

Sorbjan, Z. and Grachev, A. A.: An evaluation of the flux–gradient relationship in the stable boundary layer, Boundary-Layer Meteorology, 135, 385–405, doi:10.1007/s10546-010-9482-3, 2010.

Stull, R. B.: An Introduction to Boundary Layer Meteorology, Kluwer Academic Publishers, Dordrecht, 1997.

Thorpe, A. J. and Guymer, T. H.: The nocturnal jet, Quarterly Journal of the Royal Meteorological Society, 103, 633–653, doi:https://doi.org/10.1002/qj.49710343809, https://rmets.onlinelibrary.wiley.com/doi/abs/10.1002/qj.49710343809, 1977.